Self-calibrated Interpolation of Undersampled Non-Cartesian Magnetic Resonance Imaging Data

A DISSERTATION

SUBMITTED TO THE FACULTY OF THE GRADUATE SCHOOL

OF THE UNIVERSITY OF MINNESOTA

BY

Seng-Wei Chieh

IN PARTIAL FULFILLMENT OF THE REQUIREMENTS

FOR THE DEGREE OF

DOCTOR OF PHILOSOPHY

Advisor: Professor Mostafa Kaveh

Co-Advisor: Professor Mehmet Akcakaya

May 2021

Acknowledgements

First and foremost, I would like to thank Prof. Mostafa Kaveh for taking me under his wings as a PhD student. His support and encouragement, along with his signal processing expertise, throughout the course of my PhD research has been a key ingredient to successful completion of the thesis.

I have had the wonderful opportunity to work with my co-advisor Prof. Mehmet Akcakaya. He has provided significant input to improve my theoretical and research skills on magnetic resonance imaging. If not for his expertise providing insights and collecting clinical data, this thesis would not have been possible.

I would also want to thank Prof. Steen Moeller for his mentorship. This thesis is made largely possible due to his expertise in magnetic resonance imaging and the insightful input and training he has provided me since I joined the CMRR.

I am grateful to Professor Jarvis Haupt for serving on my PhD committee.

I thank Prof. Davide Piccini from Siemens, Prof. Matthias Stuber from Lausanne University, Prof. Gregory Metzger from CMRR, John Heerfordt from Lausanne University, Christopher Roy from Lausanne University, and Gabrile Bonanno from Siemens for the help on in vivo data collection as well as the expertise in magnetic resonance imaging.

The most important people outside of professional circles are the following three people: my father Der-Chuan Chieh, my mother Pi-Luan Wu, and my wife Cheng-

Chieh Wu. They have been extremely supportive with significant encouragement throughput my PhD journey at University of Minnesota Twin Cities.

Abstract

Effective image reconstructions from undersampled data have enabled acceleration of Magnetic Resonance Imaging (MRI) data acquisitions. Among them, the k-space reconstruction method such as Generalized Autocalibrating Partially Parallel Acquisition (GRAPPA) has been an active area of research. The k-space reconstruction of non-Cartesian sampling requires Region-specific Interpolation Kernels (RIKs) due to irregular undersampling patterns, while other types of kernels such as angularly independent/readout dependent were found to provide degraded reconstructions. The conventional strategy for calculating RIKs needs additional calibration scans, thereby increasing total scan time.

The main contribution of this thesis is to obtain RIKs without additional calibration data. The proposed method, Self-calibrated Interpolation of Non-Cartesian data with GRAPPA (SING), generates autocalibrating signal (ACS) for calibrations of different RIKs with distinct geometry patterns. A local signal-to-noise (SNR) regularization is proposed to solve linear calibration systems via regularized least-squares. The proposed regularization motivated by the inherent regularization effect of noise in through time (TT)-GRAPPA, enables a balance between the contributions of signal and noise in the estimation of the RIKs.

The SING method is validated using simulation and in vivo data, which include 2D cine, 3D whole-heart coronary, and dynamic contrast enhanced MRI prostate data. SING is also compared to reconstruction methods including gridding, TT-GRAPPA, conjugate gradient (CG)-SENSE, and compressed sensing (CS). The

experimental results show that SING has similar reconstruction performance with TT-GRAPPA without using additional calibration scans. SING enables improved reconstructions compared to gridding, CG-SENSE, and CS.

Contents

List of Figures

Chapter 1

Introduction

1.1. Background

Magnetic Resonance Imaging (MRI) uses the nuclear magnetic resonance (NMR) phenomena to enable noninvasive imaging. The gradient field, introduced by Lauterbur[1], encodes the spatial origin of the radio-frequency energy that are generated from the nuclei of the imaging object, thereby allowing for multi-dimensional imaging by NMR physics. MRI provides images with high contrast in soft tissues, as well as detailed image structures, functions, and metabolism of the organs of interest. The multi-dimensional spatial encoding can be understood by introducing the notion of k-space that describes MR sampling as Fourier encoding in two-dimensional/three-dimensional (2D/3D) spaces. The k-space sampling can be performed in Cartesian or non-Cartesian trajectories. The Cartesian sampling consists of regularly spaced points throughout the k-space, while the non-Cartesian sampling include irregularly spaced points that follow certain non-Cartesian trajectories. The k-space sampling is required to satisfy the Nyquist criterion to obtain an image without aliasing artifacts. The violation of the Nyquist criterion causes image artifacts in reconstruction.

MRI is an inherently slow imaging modality, as it acquires 2D or 3D k-space data through a sequence of 1D free induction decay signals, thereby limiting its use

especially for high-resolution or dynamic imaging. Many investigators have developed various acceleration techniques that enable reduction of the amount of acquired data without degradation of image quality. These acceleration approaches can exploit data redundancy in MRI acquisitions. For example, multiple receiver coils, which provide more useful data, have been widely used in parallel imaging techniques. Furthermore, the method for the simultaneous acquisition of spatial harmonics (SMASH[2]) was proposed and later extended to the methods including Generalized Autocalibrating Partially Parallel Acquisition (GRAPPA) by Griswold[3] and k-t space methods[4-6]. The sensitivity encoding (SENSE) technique[7] showed that spatial diversity from coil sensitivity maps have additional information that can be used to accelerate acquisitions. The data redundancy was further investigated in image or some transform domains, which is described with the concept of sparsity, for the first demonstration of compressed sensing (CS)[8, 9].

1.2. Non-Cartesian sampling

Non-Cartesian trajectories can have benefits which includes efficient coverage of k-space, fewer coherent artifacts from undersampling[10], motion robustness[11, 12], motion correction[13], self-navigation[14, 15], ultra-short TE acquisitions[16], spectrally selective imaging[17], and chemical shift imaging[18]. The non-Cartesian manner of k-space sampling includes different trajectories with different properties and implications for image reconstruction. Many non-Cartesian trajectories have been

explored, including but not limited to radial[1, 11], spiral[19, 20], rosette, BLADE/PROPELLER[13], and stochastic trajectories[21]. The combination with parallel imaging has played an important role in reducing scan times in MRI. Many acceleration imaging strategies, such as non-Cartesian parallel imaging, have been investigated to reconstruct image from non-Cartesian undersampling.

1.3. Reconstruction of non-Cartesian data

Non-Cartesian parallel imaging methods can mitigate aliasing artifacts in image reconstruction by using additional spatial encoding information from sensitivities of multi-coil phased arrays. The non-Cartesian parallel imaging approaches include Conjugate Gradient SENSE (CG-SENSE[22]), non-Cartesian GRAPPA[23-28], iTerative Self-Consistent Parallel Imaging Reconstruction (SPIRiT[29]), Partially Parallel Imaging with Localized Sensitivities (PILS[30]), parallel imaging for arbitrary trajectories using k-space sparse matrices (kSPA[31]), Parallel MRI with Adaptive Radius in k-Space (PARS[32]), parallel reconstruction Based On Successive Convolution Operators (BOSCO[33]), and Compressed Sensing (CS[9, 34]). The reconstruction of non-Cartesian data is performed in the image domain using methods including CS, CG-SENSE, SPIRiT or PILS, or in k-space with non-Cartesian GRAPPA, kSPA, PARS, or BOSCO. Reconstruction can be computed in a direct manner (non-Cartesian GRAPPA, PILS, kSPA, PARS or BOSCO), or in an iterative approach (CS, CG-SENSE and SPIRiT). The results of these algorithms can be a reconstructed image (CS, CG-SENSE, SPIRiT, and PILS), a

Cartesian k-space (SPIRiT, kSPA, and PARS), or a non-Cartesian k-space (non-Cartesian GRAPPA).

While there are many effective reconstruction approaches, as can be seen above, three representative methods are CG-SENSE, CS, and non-Cartesian GRAPPA. CG-SENSE works in the image domain using an iterative algorithm and requires coil sensitivity information. CS is a regularized version of CG-SENSE and the typical sparsity promoting regularization includes Total Variation[9] and Wavelet transform[35]. Non-Cartesian GRAPPA techniques reconstruct missing k-space data points using a direct reconstruction approach and require additional calibration data.

CG-SENSE/CS have been used in many different imaging acceleration applications, demonstrating they are robust and easily applied to different types of data. These methods do not require modifications on the sampling trajectories. The input to the reconstruction algorithm is an image reconstruction from accelerated data with arbitrary sampling trajectories. In addition, the output of the reconstruction is a reconstructed image. While CG-SENSE/CS is a commonly used parallel imaging reconstruction method, it has limitations. One challenge is the need for coil sensitivity maps, and accurate coil maps can be difficult to obtain, resulting in potential residual aliasing artifacts. Another limitation of CG-SENSE is that the stopping criteria for the iterative reconstruction is empirically defined by the user. If too few iterations are performed, the image reconstruction exhibits residual aliasing artifacts. If too many iterations are performed, the reconstructed image show visually noticeable noise amplification. One way to tackle this

limitation could be to output the image after each iteration and identify the “best” reconstruction based on an image quality metric or the user’s empirical judgement. Additionally, the selection of regularization parameter for CS/CG-SENSE is often empirical, and choosing a too small or too large parameter can lead to image quality degradation.

Non-Cartesian GRAPPA methods have beneficial properties. They are not iterative, removing the need for determining stopping criteria. In addition, the noise amplification effect of multiple coils (which is defined as g-factor[7]) for non-Cartesian GRAPPA are generally lower than Cartesian GRAPPA[36]. Through-time GRAPPA (TT-GRAPPA) enabled improvement in reconstruction of non-Cartesian data using Region-specific Interpolation Kernels (RIKs) and has been applied to radial and spiral trajectories. It has been implemented for real-time reconstruction using GPUs and distributed programming[37].

For GRAPPA, the interpolation kernels are first calibrated and then applied to undersampled data to reconstruct an image. For non-Cartesian GRAPPA, the sampling pattens are distinct throughout k-space. The calibrations of different kernels with different sampling patterns are typically performed using additional multiple calibration scans. One challenge of such calibration strategy is the increase of total scan time, thereby limiting its use especially in 3D static imaging. In addition, this poses challenges to k-space reconstruction of non-Cartesian undersampled data when calibration data are not available.

1.4. Contributions

SING (Self-calibrated Interpolation of Non-cartesian data with GRAPPA) was proposed to self-calibrate interpolation kernels for k-space reconstruction of non-Cartesian undersampled data. The AutoCalibrating Signal (ACS) were generated from linear interpolation of undersampled data in a central k-space region. Subsequently, ACS data were linearly interpolated to generate repeated non-Cartesian sampling patterns with the region-variant undersampling geometry. These patterns construct an overdetermined linear system with the GRAPPA source and target formulation. Solving for the system via locally regularized least-squares can obtain a region-specific interpolation kernel (RIK) which has distinct undersampling geometry and kernel weights over k-space. The local regularization was proposed to adapt signal contributions from noisy k-space points in the neighboring region.

The major contributions of SING include:

1) self-calibrated k-space reconstruction for non-Cartesian trajectories
2) improved reconstruction quality that matches state-of-art k-space reconstruction for non-Cartesian data
3) identified the regularization effect of additional calibration data on linear calibration system
4) adapted the signal contributions of self-calibrated kernels in noisy calibrations for improved reconstruction

1.5. Outline

The efficacy of SING was demonstrated on various non-Cartesian datasets including simulated and in vivo 2D cine imaging, 3D whole-heart coronary imaging, and 3D dynamic contrast enhanced (DCE) prostate imaging. In chapter 2, the background of cine imaging and DCE imaging are presented, as well as the challenges which the subsequent chapters aim to address. Chapter 3 focuses on 2D radial cine imaging and demonstrated the efficacy of 2D-SING along with the comparison with TT-GRAPPA. Extending 2D-SING to 3D-SING for 3D radial (kooshball) trajectories is the main topic in chapter 4. SING's applicability on 3D stack-of-stars trajectories is presented in chapter 5, focusing on 3D DCE prostate imaging. Chapter 6 provides the conclusions and the potential future work.

Chapter 2

Background

2.1. Cardiac MRI

2.1.1 Introduction

Cardiac MRI (CMR) is a medical imaging technology enabling non-invasive evaluation of functions and structures of the cardiovascular system. It is derived from the same principles of MRI but with specific modifications for the use in the cardiovascular system. The modifications include the use of electrocardiographic (ECG) gating and rapid imaging techniques or sequences. The key functional features of the cardiovascular system can be assessed combining these techniques into protocols. Using CMR provides definitive and relevant information with superior diagnostic capability without exposing to ionizing radiation. Using other non-invasive imaging techniques, including coronary CT scan, x-rays etc., rather than CMR can introduce such radiation exposure which may increase the risk of cancer and damage cells.

Gradient-recalled echo (GRE) imaging can be used in CMR since it can give T1 or T2 weighted images that imaging fibrosis and edema and black blood imaging of vascular morphology. However, morphological imaging with GRE is limited by the contrast between blood and muscle in long axis views.

In the early 2000s, the use of steady-state free precession (SSFP)[38] led to advances in the strength and linearity of imaging gradients. Balanced gradients and very short repetition time (TR) and echo time (TE) are used to achieve high signal reflecting the ratio of T2 to (T1+T2) in the steady state, thereby providing high contrast between blood and muscle as the ratio is much higher in blood than muscle. A retrospectively gated SSFP acquisition of a short axis or long axis slice can routinely be performed in a breath-hold of less than 10 s duration with negligible inflow artifacts. This technique has been primarily used in CMR at both 1.5T and 3T, while at 3T effective shimming and transmission of the excitation pulse are required to avoid off-resonance effects. The safety concerns are higher at higher field strength because energy disposition can heat the tissue. Therefore, the flip angle at 3T is reduced relative to 1.5T[39]. At higher field strengths (e.g., 7T or 9.4T) GRE is preferred to SSFP.

2.1.2 CMR techniques

Cine imaging

Cardiac cine imaging is the primary technique that characterizes regional and global contractile function of the heart and blood flow through vessels. It is of fundamental importance for clinical and research applications of CMR. When setting up a cine study, certain trade-offs that come into play when optimizing spatial and temporal resolution are SNR, scan time, breath-hold capability, and image quality.

The pulse sequence which has become the predominant cine imaging is balanced steady state free precession (bSSFP) due to its high SNR, fast imaging speed, reduced flow dependency, and high blood to myocardium contrast.

Modern CMR scanner hardware can typically achieve repetition time (TR) between RF excitations of 3-8 ms. The number of k-space lines necessary for reasonable spatial resolution of the human heart is 120-180. Even with TR of 3 ms and only 120 k-space lines, total imaging time is 360 ms. This corresponds to approximately three images per second. Such temporal resolution is too slow for the examination of cardiac contraction. The most common approach to address the limitation is segmented k-space data acquisition[40]. The image data are acquired over several consecutive cardiac cycles, and then combined during image reconstruction to produce a composite movie loop depicting a single cardiac cycle. In practice the CMR data are normally acquired while the subject holds the breath in order to eliminate respiratory motion. Total acquisition time for a single movie loop is typically 8-12 s. Breath hold image acquisitions result in move loops comprised of 16-24 frames across the entire cardiac cycle.

The parallel imaging techniques, such as GRAPPA and SENSE, provide advantages of reduction of patient breath hold durations. Multiple radiofrequency receiver coils, which contain differing spatial information, are placed around the subject’s thoracic cavity. By incorporating this information during the image reconstruction process, some k-space data can be reconstructed without acquiring them. The parallel imaging techniques represent a major advance for cine cardiac imaging with sacrifice of loss of signal-to-noise ratio.

Black-Blood CMR

CMR is often used to provide detailed information on structures including myocardium, pericardium, pulmonary veins, and emanating great vessels. When blood travels throughout the heart and blood vessels, its signal may obscure the evaluation of these structures depending on the clinical questions that are being addressed. Black blood imaging techniques aim to suppress the signal from blood, thereby improving delineation of cardiovascular anatomy. Fast spin echo-based sequences are in routine use to reduce blood flowing into the imaging plane. Such techniques have limitations that may lead to inadequate image quality or image artifacts. Recent advances have overcome some of these limitations. For example, cardiac motion may result in signal loss, and may be overcome by optimizing the cardiac phases during which the image data are acquired. Black blood imaging methods is an important tool in the CMR armamentarium, particularly with increasing prevalence of implantable devices for various cardiovascular diseases. For the bright blood imaging, devices such as intravascular stents and implantable loop recorders could generate noticeable susceptibility artifact which obscures the visualization of the anatomy of interest. Using black blood imaging can significantly reduce this artifact. The image acquisition is segmented and collected over several cardiac cycles.

Superior image quality depends on the selection of appropriate imaging parameters on a patient-by-patient basis, which is a matter of expected findings, heart rate, and the ability to hold his/her breath during the image acquisition. An

appropriate set of imaging parameters is dependent on the clinician's experience. Approaches to automate parameter selection have been introduced by the equipment manufacturers in order to improve image quality in routine clinical black-blood MRI scans[41-44].

Tissue characterization (T1, T2, T2 Techniques)*

Non-invasive characterization of tissue has been the unique domain of MRI when compared to other imaging modalities. Such techniques typically use one or more MR-based relaxation parameters and the corresponding image contrast or weighting. With or without administration of contrast agent, CMR provides detailed myocardial tissue characterization. The workhorse technique for myocardial characterization has been late gadolinium enhancement (LGE); LGE is routinely performed as an integral part of nearly every CMR exam. While originally developed to characterize infarct scar, LGE has become an important technique to delineate other features of myocardial diseases. LGE usually provides robust myocardial characterization, but has two major limitations. First, it requires administration of gadolinium-based contrast, which may not be suitable for individuals with allergy to such agents or patients with advanced kidney disease. Second, it may be insensitive to more diffusely diseased myocardium. To overcome these limitations, and characterize other myocardial features, imaging techniques that capture intrinsic contrast in T1, T2, and other MR-based relaxation parameters are often incorporated into the CMR examination. The approaches,

also known as tissue mapping techniques, enable further advance MR-based myocardial characterization.

The basic CMR clinical scan usually includes cine function, myocardial perfusion under rest and/or stress and, last but not least, tissue viability imaging. In most clinical cases, images are interpreted based on image contrast. However, research has shown that there are advantages to collecting quantitative data rather than relying on image contrast[45]. For instance, quantitative techniques have the advantage of providing absolute values for quantifying abnormalities. This is useful especially in diseases where the entire heart is affected, and diagnosis cannot rely on localized tissue contrast[46]. In tissue mapping, every pixel of the image contains the value of a tissue relaxation parameter, such as T1, T2, or T2*.

The collection of T1-weighted images either with or without contrast agents can produce clinically useful images, while it becomes more complicated in the presence of cardiac and respiratory motion. The most commonly used T1-weighted imaging sequence is T1-weighted so as to depict normal myocardium dark and infarcted myocardium bright. The contrast between normal and infarcted myocardium is based on the premise that 20 min after intravenous administration the contrast agent distributes not only in the extracellular but also in the intracellular space in acutely infarcted myocardium.

Tissue characterization methods are developing rapidly. It makes MRI different from other imaging techniques and is likely one that will benefit future clinical applications.

Perfusion

Myocardial perfusion is an important measurement in the diagnosis of coronary artery disease. MRI has recently emerged as a method with many advantages. Compared to single proton emission computed tomography (SPECT), MRI has much higher resolution, requires no radiation dose, and has the potential for more quantitative measurements. However, MR perfusion measurement can be complex. There are a variety of choices to consider when designing a MR perfusion experiment. However, there is no consensus MRI perfusion implementation that is best for all situations, and selecting the ideal parameters for a given scan needs a careful understanding of the pros and cons of each component of an MRI perfusion experiment.

The choice of pulse sequence is a key determinant of image contrast, spatial and temporal resolution, coverage, and degree of artifacts. These characteristics are usually at odds with one another. For example, gain in contrast may come at the expense of resolution or coverage. Selecting the optimal sequence requires weighing these competing gains and losses against each other. In meeting these requirements, perfusion imaging has a critical constraint that is absent in much of CMR. The segmented acquisition (as is used in cine and LGE imaging) is limited or impossible because characterizing the bolus passage requires the acquisition of a full image everyone to two heart beats. In order to achieve full heart coverage, three short axis images typically must be acquired within the time course of a single heartbeat. This limits perfusion imaging to very time-efficient pulse sequences that

reduce the time to acquire an image to ~100 ms. Currently, the majority of CMR perfusion scans are acquired using saturation recovery (SR) preparation. Critically, SR pulses have no heart rate dependence since it sets M_z to zero regardless of the prior M_z. In addition, more slices can be acquired allowing for greater spatial coverage because the readout is faster. The magnetization preparation pulse can be combined with different types of image readout. The most common types are ultra-fast gradient echo[47] (e.g. TurboFLASH, fast GRE, and Turbo Field Echo), gradient echo with echo planar readout[48] (GRE-EPI), or steady state free precession[49] (SSFP). Despite of much debate, there is no clear consensus for which sequence is optimal for CMR perfusion and is usually determined based on the preference of the physician.

Due to the need for very fast image acquisition, cardiac perfusion sequences are almost run with an acceleration technique including parallel imaging (e.g. SMASH[2], SENSE[7], and GRAPPA[3]). In most centers, a wider adoption of multi-coil arrays supports the use of parallel imaging techniques[50]. Practically, the acceleration provided by these methods is limited to two to three-fold due to increasing SNR penalties with higher acceleration rates[51]. Prior-knowledge driven methods such as k-t Broad Linear Speed up Technique (BLAST) and k-t SENSE[4] and Highly Constrained Back-Projection Reconstruction (HYPR[52]) allow higher acceleration with relatively preserved SNR[53, 54]. In addition, compressed sensing emerges as a promising method to accelerate myocardial perfusion CMR[55]. The speed up in the data acquisition enables the increased spatial resolution or increased cardiac coverage.

Stress Testing

Stress imaging has become a major CMR application in which practice guidelines recommend its use in various clinical scenarios. The indications of stress CMR include imaging of patients with suspected coronary artery disease (CAD) and patients with heart failure and cardiomyopathy. The commonly used stress method in CMR is vasodilator stress combined with dynamic first pass contrast enhanced perfusion imaging, while inotropic and physiological stress which detect either perfusion or wall motion abnormalities are also suitable. When performing stress CMR, additional safety considerations are considered due to the potential of inducing cardiac arrhythmias or causing ischemia. The challenges in designing pulse sequence relate to the fast heart rates encountered and the need in dynamic first pass perfusion to capture image data with high spatial and temporal resolution. The current trends include developing higher spatial resolution and three-dimensional methods for myocardial perfusion CMR.

Images are acquired in multiple planes (typically at least three short axis and two orthogonal long axis planes) at each stress level. The stress CMR methods used for stress wall motion imaging are similar to those used in standard cine imaging. The retrospectively gated balanced steady state free precession (bSSFP) cine pulse sequences are normally used. Adjustments to the standard pulse sequence may be made to allow for higher heart rates and reduced breath-hold capacity during stress testing. The objective of pulse sequence design is to achieve a breath hold duration of 4-6 s, temporal resolution of >25 phases/cardiac cycle and in-

plane spatial resolution of 1.5-2×1.5-2 mm with a slice thickness of 8-10 mm[56]. To achieve these requirements, the adjustments that are often made include:

- Use of parallel imaging (allowing acquiring fewer k-space lines and thereby reducing acquisition time)
- Reduced temporal resolution (more k-space lines can be acquired in each cardiac phase)
- Reduced spatial resolution (smaller image base matrix is used at similar field of view, resulting in fewer required k-space lines)

Many other adjustments can be made and with a combination of these, real time cine acquisition and monitoring can be achieved[57].

On current scanners, bSSFP sequences are typically used to provide high SNR, while enabling a good contrast between the blood and the myocardium without suffering from flow related artifacts. The elevated SNR for bSSFP allows the use of parallel imaging with higher acceleration rates, resulting in high speed and high contrast acquisitions and a significant reduction of breathing artifacts, particularly if the images are acquired in the end-expiratory phase. These properties make bSSFP cine imaging particularly useful during stress testing. However, bSSFP sequences are very sensitive to off-resonance artifacts in high field strength and with rapid blood flow. For example, image artifacts can be noticeable in descending aorta with the four-chamber view. Modifying the phase encoding direction and more accurate shimming can significantly reduce the occurrence and extent of these artifacts.

Late Gadolinium Enhancement

Late Gadolinium Enhancement CMR (LGE-CMR) has become the gold standard tool for a wide range of myocardial abnormalities, most commonly infarct scar but also fibrosis of nonischemic disease and inflammatory and other infiltrative materials. LGE image acquisition occurs at a set delay (10-15 min) following the intravenous injection of gadolinium-based contrast media, in order to capture a 'snapshot' of the extravascular-extracellular distribution of contrast.

The penetration of the LGE imaging technique into mainstream imaging protocols is primarily improvement and innovation in MR hardware (gradient performance, RF coil sensitivity) and pulse sequence design. The pulse sequences used in scanners today provide sufficient contrast-to-noise ratio (CNR) and spatial resolution to resolve not only subendocardial infarcts, but post-ablation scars in the left atrium. In the 1980s the initial LGE studies consisted of inversion-prepared spin-echo and fast ("turbo") spin-echo sequences[58-60]. Although the sequences provided the T1-weighting needed for delineating areas of gadolinium accumulation, the acquisition times were long, thereby making breath-hold impractical or impossible. Images were degraded by respiratory artifacts. In the mid-to-late 1900s most of spin-echo sequences had been replaced by faster gradient-echo varieties. Saturation-[61] or inversion-[62] preparation provided the T1-weighting, along with short TR and shallow flip angle readouts. The gradient-echo techniques offered several advantages, because they were sufficiently rapid acquisition within a reasonable breath-hold and could be repeated comfortably to

follow the temporal evolution of contrast accumulation. The single-shot saturation-prepared fast gradient-echo sequence was, in fact, used for both perfusion and LGE imaging. They could be acquired either with or without a breath-hold, depending on the post-processing performed in the quantitative analysis.

LGE imaging has evolved to an essential component of most clinical CMR examinations. The pulse sequence and implementation may differ depending on availability and indication, firm understanding of the principles underpinning LGE will assist in offering important diagnostic information relevant for patient care.

Flow imaging

MRI technique enables the quantitative measure of blood velocity and the determination of blood flow[63] and Phase-Contrast Magnetic Resonance (PCMR) is the most commonly used approach to quantify blood flow. Other MRI-based methods for quantification of velocity flow include blood labelling, but they are not often used[64].

The majority of implementations of PCMR need a rapid, low flip angle, gradient echo sequence. The sequence employs a short TR and a short TE to minimize se-phasing in the presence of complicated flow and to increase temporal resolution when cardiac gating is used[65]. Lower flip angle reduces radiofrequency energy deposition and keeps TE as short as possible. In order to reduce acquisition time, segmented acquisitions are often employed to acquire several k-space lines/projections for each cardiac phase. The larger the number of k-space

lines/projections that are acquired per cardiac phase, the shorter the overall acquisition time. The penalty for shortened overall acquisition time is reduction of temporal resolution. Variations on the pulse sequence include echo-planar techniques[66], spiral readouts strategies[67], and SSFP[68].

CMR is routinely used in a variety of cardiovascular abnormalities to quantitatively measure blood velocity and determine flow. PCMR is the most commonly used technique. Clinical applications include valvular heart disease, congenital heart disease, vascular disease and myocardial disease.

2.2. Dynamic Contrast Enhanced imaging (DCE)

2.2.1 Introduction

MRI has enabled the diagnosis, grading and classification of tumors and has become essential to the adequate clinical management of many tumor types. The ability of MRI to demonstrate tumor morphology and the relationships of malignant lesions to neighboring structures provides essential clinical information. MRI has innate advantages in these applications enabling clear delineation of normal anatomical structures and organs, as well as clear identification of pathological change. The development of small molecular weight paramagnetic contrast agents has had a major impact on the application of MRI in oncology. Many tumors exhibit

distinctive enhancement patterns which may provide useful diagnostic or staging information.

2.2.2 Pulse Sequences

Typical clinical MRI scanners can offer a variety of pulse sequences which are suitable for DCE imaging. The selection of pulse sequence is determined by the comprise between imaging time, spatial resolution, anatomical coverage, sensitivity to artifacts, SNR, and degree of contrast weighting. T1-weighted DCE-MRI is most commonly acquired using gradient echo-based sequences. The typical gradient echo sequences include GRASS, FISP or FFE[69], T2-weighted sequences called T2-FFE or PSIF[70], T1-weighted sequences (spoiled GRASS, T1 FFE or FLASH)[71] and the methods which applied balanced gradients (FIESTA, balanced FFE, or True FISP)[72]. Balanced gradient echo sequences have high sensitivity to T2 effect, and this is undesirable as the signal decreases once contrast agent arrives at the tissue. Many dynamic studies have therefore used spiled gradient echo sequences that are more sensitive to T1 effect and therefore show signal increases. The main problem with these techniques is low SNR which can be compensated to some extent by the use of 3D acquisitions. The transient gradient echo sequences combine a contrast preparation pulse with a sequence for image readout, allowing control over the contrast sensitivity. T1 sensitive versions of transient gradient echo techniques have been used extensively in DCE-MRI.

2.2.3 Analysis

A large range of techniques have been applied to analyze the signal enhancement curves observed in DCE-MRI. They range from simple visual inspection to complicated quantification with pharmacokinetic models. These analysis methods are based on measurements from user-defined region of interest. While this simplifies the use, the disadvantages include variability and potential intra observer errors. It may lead to incapable identification or quantification of significant heterogeneity within tumor microvascular within the region of interest.

The optimal analysis of DCE-MRI data would be designed to identify specific quantitative physiological parameters which describe the tissue microvasculature which is being observed. The distribution of contrast material is governed by regional blood flow, blood volume, vessel shape and size, endothelial permeability and the size of extracellular extravascular space. Many groups have described approaches which derive these parameters from the changes in signal intensity that occur during contrast passage[73-78]. The type of analysis method requires the application of a quantitative mathematical model describing the pharmacokinetics of contrast agent. In order to apply pharmacokinetic models of contrast distribution to image data, the signal changes observed in the dynamic acquisition is used to calculate quantitative parametric images of contrast concentration at each time point. The relationship between signal intensity and contrast concentration may be non-linear, which adds additional complication and often requires the

measurement of the pre-contrast T1 values at each voxel. Then a parametric image of T1 corresponding to the dynamic time course is generated. Using these quantitative T1 images along with the observed signal change, each of the dynamic series images can be transformed to a parametric image of contrast concentration. These contrast concentration time course curves for individual voxels are then used as the substrate for pharmacokinetic models.

A variety of pharmacokinetic models have been applied to analyze DCE-MRI data. Most of models use curve fitting methods to estimate the parameters. Although more complicated models can describe all of the physiological features, the instabilities in the analysis and the increasing estimation errors of the parameters may be observed. This has led to the development of simplified models that combine the effects of several parameters into one in order to reduce the number of variables used in curve fitting. Most studies[73-78] focus on the calculation of the contrast transfer coefficient K^{trans}. A simpler model estimates only two parameters[79], which are the size of extravascular-extracellular space (v_e) and K^{trans}. The coefficient K^{trans} is affected by flow, endothelial permeability, endothelial surface area product and by the proportional blood volume of the voxel. High values of K^{trans} are seen where there is high flow, high permeability, high capillary surface area or a large proportional of intravascular contrast within the voxel. While the measurement is highly non-specific, it is reproducible and provides a quantitative measurement of microvascular structure and function, resulting in a wide use in many studies.

DCE-MRI involves the acquisition of images before, during, and after the injection of a contrast agent. In order to perform quantitative modeling on the resulting signal intensity time course, data must be acquired rapidly, leading to compromises in spatial resolution, SNR, and field of view. One strategy that may allow gains in temporal or spatial resolution or SNR of images is compressed sensing (CS).

2.3. Acceleration methods

2.3.1. Dynamic acquisitions

Dynamic imaging benefits from both high temporal and high spatial resolution as well as high SNR; high temporal resolution is needed for quantitative analysis, and high spatial resolution aids clinical reading. However, the requirement of high SNR images limits simultaneous high temporal and high spatial resolution when using conventional data acquisition strategies. The acceleration of dynamic imaging is a common approach used to balance the trade-off between spatial and temporal resolution. The data is undersampled in the k-space. Parallel imaging, including SENSitivity Encoding (SENSE)[7, 51] and GRAPPA[3], are the common acceleration techniques.

For the applications in CMR, the accelerated imaging is essential in order to capture the rapid motion of the heart and blood. The acceleration rates of up to 6 or 7 using a 32-channel receiver coil have been shown[80, 81], but higher acceleration in 2D imaging is generally not possible because of the SNR loss due to the geometry factor. Higher acceleration factors have been demonstrated in 3D by

accelerating in both the phase and partition encoding directions[82]. The standard parallel imaging methods require a low-resolution calibration dataset to determine either the coil sensitivity map needed for SENSE or the interpolation weights needed for GRAPPA. In dynamic imaging, this requirement can be avoided by interleaved undersampling in TSENSE or TGRAPPA[83, 84]. The methods, such as UNFOLD or k-t BLAST[4] (Broad-use Linear Acquisition Speed-up Technique), take advantage of the spatiotemporal correlations inherent in cardiac movement to offer data reduction, but are plagued by temporal blurring. K-t SENSE or k-t GRAPPA[4, 85, 86] provided improved accelerations.

Several early DCE-MRI acceleration studies include keyhole[87], k-t Focal Underdetermined System Solver (FOCUSS[88]), k-t BLAST and k-t SENSE[4]. In the keyhole imaging, a subset of low-frequency data around center of k-space is collected, while high spatial frequency data is acquired less frequently. As such, the data acquisition time on average is reduced. The low-frequency data are then combined with the high-frequency data to generate a composite full resolution image that captures dynamic changes. This keyhole technique has been widely employed in clinical MRI[89]. However, these methods suffer the limitations including low SNR and aliasing artifacts at high acceleration rates.

Compressed sensing (CS) is a suitable reconstruction technique in dynamic MRI, as the temporal correlations provide data sparsity in addition to spatial sparsity. The feasibility of CS framework was assessed for accelerated dynamic MRI with computer simulation, in vivo fully-sampled cardiac data and Fourier velocity encoded imaging[90]. For the acceleration of perfusion CMR, a joint sparsity of

multicoil images in spatial and temporal directions can be exploited to combine CS and parallel imaging to accelerate CMR perfusion[55]. Other advanced CS technique include the use of sparsity regularization on localized information in both spatial and temporal dimension[90, 91]. For the applications in cine imaging, CS reconstruction and parallel imaging techniques including GRAPPA are applicable to evaluate left ventricular function and volumes with high accuracy[24, 26, 92, 93].

CS has also been applied to DCE-MRI to provide improved reconstruction performance compared to earlier methods, serving as a potential tool for cancer MRI[94]. Other CS studies include k-t SPARSE[95], k-t Sparse and Low Rank[96] (SLR) and Golden-angle RAdial Sparse Parallel MRI[97] (iGRASP). As a variant approach, a difference operator applied to temporal frames was shown to enhance the spatial signal sparsity for CS reconstruction[98].

2.3.2. Static acquisitions

The static or anatomic imaging in MRI enables non-invasive diagnosis among patients with suspected coronary arteries disease, prostate cancer (evaluation, detection and staging), etc. Coronary artery MRI has evolved as a non-invasive diagnosis alternative to catheter based x-ray angiography among patients with suspected anomalous coronary artery disease and coronary artery aneurysms[99]. Although coronary multi-detector computed tomography (MDCT) provides superior isotropic spatial resolution and rapid imaging, coronary MRI is advantageous to MDCT in several respects, including the absence of ionizing radiation which

facilitates follow-up scanning and smaller artifacts related epicardial calcium. With these advantages offered by coronary MRI along with its diagnostic accuracy, it is recommended as appropriate in patients who are suspected of anomalous coronary artery disease by both the American College of Cardiology and American Heart Association[100, 101].

The early approaches to coronary MRI are based on 2D breath-hold

electrocardiogram (ECG) triggered segmented sequences[102]. Over the past two decades, 3D free-breathing approaches have replaced 2D acquisitions due to greater anatomical coverage and higher signal level. Targeted[103-106] or whole-heart[107-121] coverage of the coronary anatomy is possible in 3D coronary MRI. Both GRE and SSFP have been used for targeted 3D coronary MRI[122, 123]. For while-heart coronary MRI, SSFP appears to be the sequence of choice because of its higher blood-myocardium contrast and superior inflow properties[124].

The clinical acceptance of coronary MRI remains challenging due to coronary artery motion, long scan times, limited spatial resolution, suboptimal SNR and blood-myocardium contrast-to-noise ratio (CNR). To overcome some of these limitations, the approaches including non-Cartesian sampling, accelerated imaging, and higher field strength have been developed.

Non-Cartesian trajectories provide efficient k-space traversals and less visually significant artifacts than Cartesian. The suitable non-Cartesian acquisition include spiral[20] and radial. For radial trajectories, data in healthy subjects appear promising[35, 122, 125] and may be beneficial for coronary wall imaging[126, 127].

Parallel imaging techniques such as SENSE[7, 51] or GRAPPA[3] are the most commonly utilized clinical acceleration methods for coronary MRI[108, 128-130]. The resultant acceleration rates of up to twofold when using 16-coil array and up to fourfold when using 32-coil array have been accomplished[116, 131].

CS method has emerged as an alternative acceleration strategy which exploits the sparsity of image in transform domain[8, 9]. CS also needs incoherent undersampling pattern which can be achieved by random undersampling in k-space with 3D Cartesian acquisition. For high-resolution coronary MRI, an advanced CS shown improved reconstruction with reduced blurring compared to conventional CS[132], and was utilized in contrast-enhanced whole-heart coronary MRI[133]. As for highly-accelerated sub-millimeter resolution whole-heart coronary MRI, CS outperforms parallel imaging at acceleration rate of 6 in a head-to-head comparison[134]. CS can also be combined with non-Cartesian imaging, such as spiral[135] or 3D radial[35], to enable whole heart acquisitions.

Chapter 3

2D Self-calibrated Interpolation of Non-cartesian data with GRAPPA (SING)

3.1. Background

3.1.1. Region-specific Interpolation Kernels (RIKs)

K-space reconstruction of 2D non-Cartesian undersampled data has been demonstrated using non-Cartesian GRAPPA[10, 136-143]. In non-Cartesian undersampling, each local region of undersampled k-space has a distinct sampling pattern with varying distribution of acquired k-space points, thereby requiring region-specific interpolation kernels. The RIKs proposed by TT-GRAPPA have enabled promising non-Cartesian reconstruction for non-Cartesian dynamic imaging in clinical studies[26, 142, 144-147]. The TT-GRAPPA method calibrates each RIK by using additional non-Cartesian calibration scans from which sufficient numbers of repeated sampling patterns for each RIK with the distinct geometry are obtained. However, RIKs are challenging to be calibrated when additional calibration scans are not available.

Recently, self-calibrated non-Cartesian GRAPPA methods have been proposed to obtain RIKs without the need of calibration scans. Our early study demonstrated a self-calibration strategy, namely Adaptive Interpolation functions for Multichannel MR system (AIM), using spatially smooth functions such as coil sensitivity maps or cosine functions[148]. The multiplication between composite multicoil images and the smooth functions in image space corresponds to the interpolation of composite data for the generation of ACS data. The schematic is illustrated in Figure 1. Each RIK is calibrated using ACS data in the local k-space region which it applies to for the reconstruction. While this approach has shown promising reconstructions, the recons improvement could be made using ACS data with higher SNR. In the AIM method, RIK for undersampling region far from k-space center is calibrated using ACS data with low SNR. To calibrate RIKs with higher SNR calibration data, our newer SING method is proposed to utilize ACS data around center of k-space.

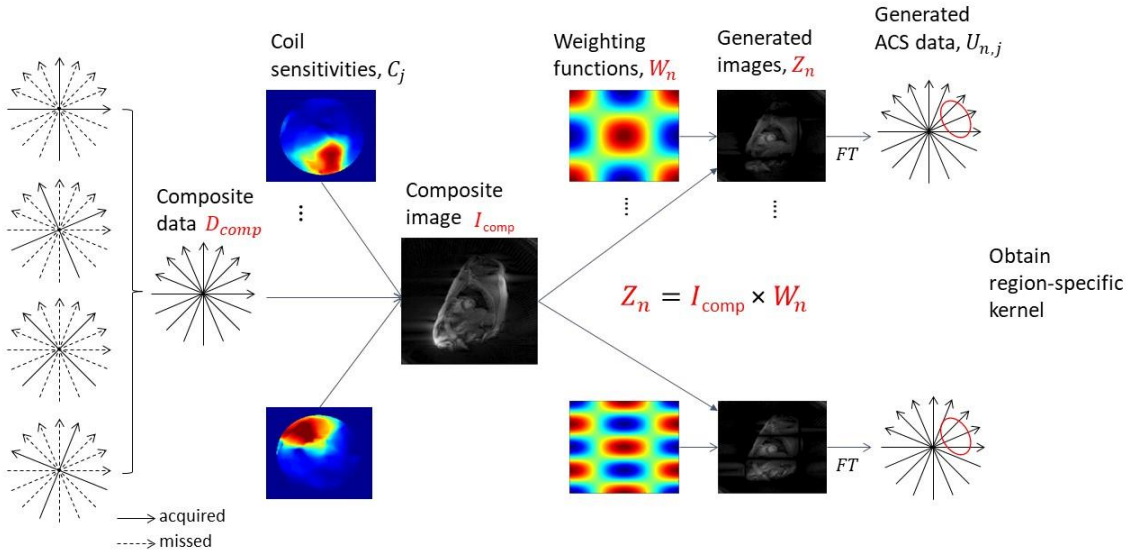

Figure 1: The schematic of AIM method. The multiplication of the sensitivity-combined composite image I_{comp} and the spatially smooth weighting functions W_n can generate ACS data which is interpolated from the composite data D_{comp}. The calibration of each RIK is performed using its neighboring ACS data.

Alternatively, Luo et al.[149] has shown that each RIK can be calculated from a Cartesian ACS region, which is either acquired or reconstructed from a non-Cartesian data set by applying selected linear phase modulations in image space and then transforming to k-space through fast Fourier transform to obtain repeated non-Cartesian sampling patterns necessary for calibration of each RIK. The performance of the self-calibrated RIK in the work by Luo et al was found to match the reconstruction quality of CG-SENSE.

In this chapter, 2D-SING is introduced to obtain an overdetermined calibration system and a different estimation for each RIK. A local k-space regularization for the calibration of RIKs, extended from inherent regularization effect in TT-GRAPPA, is proposed to match the reconstruction quality of TT-GRAPPA.

3.2. Method

3.2.1 Generate ACS data

The flowchart of 2D-SING is illustrated in Figure 2.

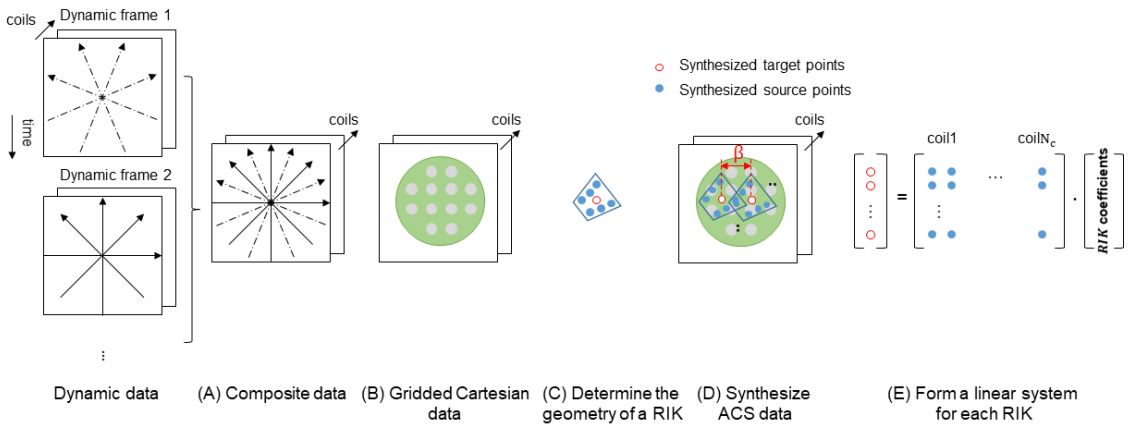

Figure 2: The schematic of SING forming a linear calibration system for a RIK. The ACS data on Cartesian grid is generated from the acquired dynamic data (A)-(B). The ACS data is then interpolated to synthesize RIK sampling patterns which form a linear calibration system. The calibration of a different RIK is performed by repeating the steps (C)-(E).

Dynamic non-Cartesian measurements in each channel are combined, independently of other channels, into a composite data set with lower temporal resolution as shown in Figure 1A. The composite non-Cartesian measurements in each channel are resampled, independently of other channels, with density compensation, convolution with a Kaiser-Bessel function[150] of width $L = \Delta k$ (Δk is Nyquist sampling interval in k-space), and resampled on Cartesian points. The region with the resampled Cartesian points from Nyquist sampled non-Cartesian data, shown as a circular region in Figure 1B, is referred to as the ACS region.

To extract one calibration equation, the target and source points are synthesized by convolving the resampled Cartesian points with a Kaiser-Bessel function with

width $L = \Delta k$ and then resampling at the locations that match the sampling pattern with a distinct shape for a RIK. The same sampling pattern is shifted vertically and horizontally relative to the first sampling pattern by a distance $\beta \geq L$ over the ACS region until all of the gridded Cartesian points are used to extract additional calibration equations, as illustrated in Figure 1D. Using all extracted equations, a linear overdetermined system with the GRAPPA source and target formulation for calculating a RIK can be established and be solved to determine the signal correlations for GRAPPA interpolations in the local k-space region corresponding to a RIK, as specified in Figure 1E. The synthesis of target and source points is repeated to calibrate other RIKs until all local k-space regions with missing points are interpolated. If β is smaller than L, the Kaiser-Bessel convolution results in correlations among adjacent patterns and negatively affects the conditioning of the calibration system.

Each RIK is the least-squares solution of a linear calibration system

$$arg\min_{\mathbf{x}} \|\mathbf{b} - \mathbf{A} \cdot \mathbf{x}\|_2^2, \quad (1)$$

where $\mathbf{b}$ is an M×1 vector of target points, $\mathbf{A}$ is an M×N matrix of source points, and $\mathbf{x}$ is an N×1 vector of the coefficients in the RIK.

3.2.2. Local k-space regularization

Noise amplification in the estimation of a RIK via least-squares, which is determined by the conditioning of the linear system, can lead to noise-like errors in the image reconstruction. Tikhonov regularization has been used to mitigate noise amplification in kernel calibrations[151], but it often results in blurring artifacts in image reconstruction[152]. Furthermore, tuning a single regularization parameter for each RIK using the discrepancy principle or the L-curve method. requires multiple calculations of a matrix inversion, and as the parameter tuning is repeated for different RIK, such a tuning process requires significant computations.

To develop a strategy with improved sharpness in image reconstruction that is comparable to TT-GRAPPA, we investigate the effect of SNR in calibration data on k-space reconstruction. Several studies have demonstrated that lower SNR ACS data can be advantageous for GRAPPA reconstruction[153, 154]. Furthermore, it was shown that adding noise onto the source matrix (matrix $\mathbf{A}$ in Equation 1) for determining interpolation kernels has the same effect as Tikhonov regularization[155]. For the RIK calibrations in TT-GRAPPA, where local k-space is used for calibrating each RIK, the variable SNR in k-space as such implicitly regularizes each RIK in TT-GRAPPA differently.

Motivated by the regularization effect from noise inherent to TT-GRAPPA, we propose a local k-space regularization by using local SNR level in k-space. The definition of local signal level is the l_2 norm of acquired k-space points across all channels in the local region where a RIK is applied for k-space interpolation. By proposing the use of local k-space SNR level for regularization, the computationally intense parameter tuning with discrepancy principle or L-curve

can be eliminated. The proposed regularization adds noise to the calibration system of each RIK, matching the SNR effect of through-time calibration data on RIK calibrations in TT-GRAPPA. Before adding noise, the system is as specified in Equation 1. After adding noise, similar to what is done implicitly in TT-GRAPPA, the system is represented as

$$\min_{\mathbf{x}} \|(\mathbf{b} + \Delta\mathbf{b}) - (\mathbf{A} + \Delta\mathbf{A}) \cdot \mathbf{x}\|_2^2. \quad (2)$$

We propose to determine the variance of $\Delta\mathbf{b}$ and $\Delta\mathbf{A}$ to match the SNR between the synthesized ACS points and the measured k-space points in the local region of k-space

corresponding to each calibrated RIK. For the source and target points of a mth sampling pattern in the ACS, the variance of $\Delta\mathbf{b}$ and $\Delta\mathbf{A}$ is calculated with the SNR of these points to the undersampled signals in the local region corresponding to each RIK, scaled by the standard deviation of the thermal noise σ as

$$w_m = \sigma \cdot \frac{a_m}{u}, \quad (3)$$

where a_m is the SNR level of source points of the mth pattern in the ACS (mth row in matrix $\mathbf{A}$ in Equation 1), calculated with the l_2 norm of these points across all

channels, and u at the SNR level in the local region of acquired k-space where applying each calibrated RIK for k-space interpolation is sought, calculated as the l_2 norm of neighboring acquired signals across all channels. Thus, $\Delta\mathbf{b}$ and $\Delta\mathbf{A}$ are generated as

$$\Delta\mathbf{b} = \mathbf{W} \cdot \boldsymbol{\chi}$$

$$\Delta\mathbf{A} = \mathbf{W} \cdot \mathbf{X}, \quad (4)$$

where the entries of $\boldsymbol{\chi}$ and $\mathbf{X}$ are drawn from a standard normal distribution, and $\mathbf{W}$ is an M×M diagonal weighting matrix with the diagonal entry w_m as specified in Equation 3.

The coefficients of each RIK are obtained by solving Equation 2 via least squares and then used to recover the missing data points in the local region of undersampled k-space corresponding to each RIK. The reconstructed fully sampled multichannel non-Cartesian data are transformed to image space via gridding reconstruction channel-by-channel, and a reconstructed image is obtained with the root sum of square channel combination.

3.2.3. Numerical simulations

The MRXCAT[156] cardiac numerical phantom was used for the simulations. Thirty synthetic coil sensitivity profiles were simulated from an in vivo cine imaging data set and added to the MRXCAT simulation. For each cardiac phase, a multichannel radially fully sampled k-space with 216 radial projections was generated using

inverse gridding on the individual coil sensitivity weighted phantom image under simulated breath-hold. Complex white Gaussian noise was added to yield an SNR of 40 calculated over the image object. An angularly uniform radial pattern was used to undersample the k-space in each cardiac phase, and the bit-reversed ordering was used as the interleaved undersampling ordering throughout cardiac phases to suppress simulated motion effects. Twenty free-breathing fully sampled noisy radial k-space data sets, added with the noise of the same distribution in the numerical undersampled data specified previously, were generated using the cardiac phantom images under simulated free-breathing provided by the MRXCAT simulated data sets for TT-GRAPPA calibration purposes.

3.2.4. In vivo imaging

The imaging protocols were approved by the local institutional review board, and the written informed consent was obtained from all subjects before each scan of this HIPAA-compliant study. Cine cardiac MRI was acquired at 3 T (Siemens Prisma) on 2 healthy subjects using a 30-channel body array with a gradient-echo sequence using the following imaging parameters: TE/TR/α = 2.3 ms/3.9 ms/12°, bandwidth = 440 Hz/pixel, in-plane resolution = 2 × 2 mm^2, and FOV = 300 × 300 mm^2. The readout sampling rate was 2 times the acquisition bandwidth, and the number of total sampled readouts in each radial projection was 288. The fully sampled radial data set in each cardiac phase contained 216 radial projections using a linear view order in a single breath-hold acquisition. During each cardiac

phase of a heartbeat, 9 radial projections were acquired in a linear order to yield a temporal resolution of 35 ms for the fully sampled cardiac images. Data were retrospectively undersampled in a uniform angular pattern for each cardiac phase with bit-reversed ordering for interleaved undersampling to suppress motion effect throughout cardiac phases, and the undersampled data were used for reconstruction. For TT-GRAPPA calibrations, additional 20 free-breathing fully-sampled acquisitions were obtained shortly after the breath-hold acquisition.

3.2.5. Effect of inclusion of central ACS region on calibration

The effect of using the central ACS, which yields residuals of high magnitudes in the calibration system due to high signal variations[157] on SING, was investigated by performing 2 SING calibrations that included and excluded these central ACS points and then reconstructing 2 sets of images using 2 sets of RIK corresponding to these 2 calibrations. The central ACS region was defined as a circular region with a radius of $\gamma \cdot \Delta k$, and different values of γ of 2, 4, 8, 12, and 16 were evaluated. The proposed local k-space regularization was used on all SING calibrations.

3.2.6. Effect of regularization on SING calibration

The regularization effect on RIK was evaluated by performing SING calibration with no regularization, Tikhonov regularization, and the proposed signal-based

regularization. Tikhonov regularization parameters were chosen in a readout-dependent manner based on the decay rate of Fourier coefficients along the readout dimension. For each RIK, the Tikhonov parameter was chosen as

$$\sigma \cdot \left(\frac{\mathrm{r_{miss}}}{\mathrm{r_{ACS}}}\right)^{\mathrm{q}}, \quad (5)$$

where σ is the standard deviation of thermal noise, q is a positive scalar and empirically optimized to q=2 after visually inspecting reconstructed images for q values from 1 to 3, $\mathrm{r_{miss}}$ denotes the readout coordinate of the missing data points reconstructed using the RIK, and $\mathrm{r_{ACS}}$ denotes the averaged readout coordinate of sampling patterns in the ACS region.

3.2.7. Reconstruction evaluation

CG-SENSE[22], TT-GRAPPA, and SING methods were compared in numerical simulations and in vivo imaging. Two acceleration rates R of 6 and 12 were included. The CG-SENSE method was implemented with Tikhonov regularization, in which the regularization parameter was empirically set to λ= 0.1 for both R = 6 and R = 12 after visually inspecting the reconstructed images for λ values from 0.001 to 1. The stopping criterion was implemented to minimize the relative l_2 norm difference between two subsequent iteration images to less than 1%. The coil sensitivities were calculated from gridding reconstructed fully sampled coil images using ESPIRiT[158]. In TT-GRAPPA, each RIK with size 2 × 5 (angle × readout) was

estimated using the local through-time acquired calibration data points in the neighboring region spanning ± 4 readouts samples, spanning $2\Delta k$ (Δk: Nyquist sampling interval) in the readout dimension, and ± 4 projections similar to the original proposed approach. The size of this neighboring region was empirically validated after testing TT-GRAPPA reconstructed images corresponding to different sizes with $\pm i \times \pm j$ (readouts × projections) for i, j=2,4,6,8. In SING, the gridded Cartesian points (gridded with oversampling ratio of 2 from fully sampled non-Cartesian acquisitions) in the central region of size $60\Delta k \times 60\Delta k$ and $72\Delta k \times 72\,\Delta k$ are used for R = 6 and R = 12, respectively, to obtain an 8-times overdetermined linear system for calculation of the RIKs. For k-space reconstruction, each RIK was used to reconstruct 2 samples angularly positioned between the 2 acquired projections, and 4 samples radially, as used in TT-GRAPPA. Specifically for the data used, the corresponding number of RIKs is 180*288/8 = 6,480 at R = 6 and 198*288/8 = 7,128 at R = 12 (R being the acceleration rate), respectively, where 180 and 198 denote the number of missing radial projections at R = 6 and

R = 12, respectively. For each reconstructed image, both the difference image and the normalized RMS error were computed with respect to the gridding reconstruction of the fully sampled acquisition (the reference image). G-factor maps were calculated using the pseudo-replica method[159] with 5000 iterations for CG-SENSE, TT-GRAPPA, and SING.

3.3. Results

3.3.1. Effect of inclusion of central ACS region on calibration

Figure 3 shows 2 sets of reconstructed images corresponding to 2 SING calibrations that included and excluded the central ACS region in the numerical simulation and an in vivo data set.

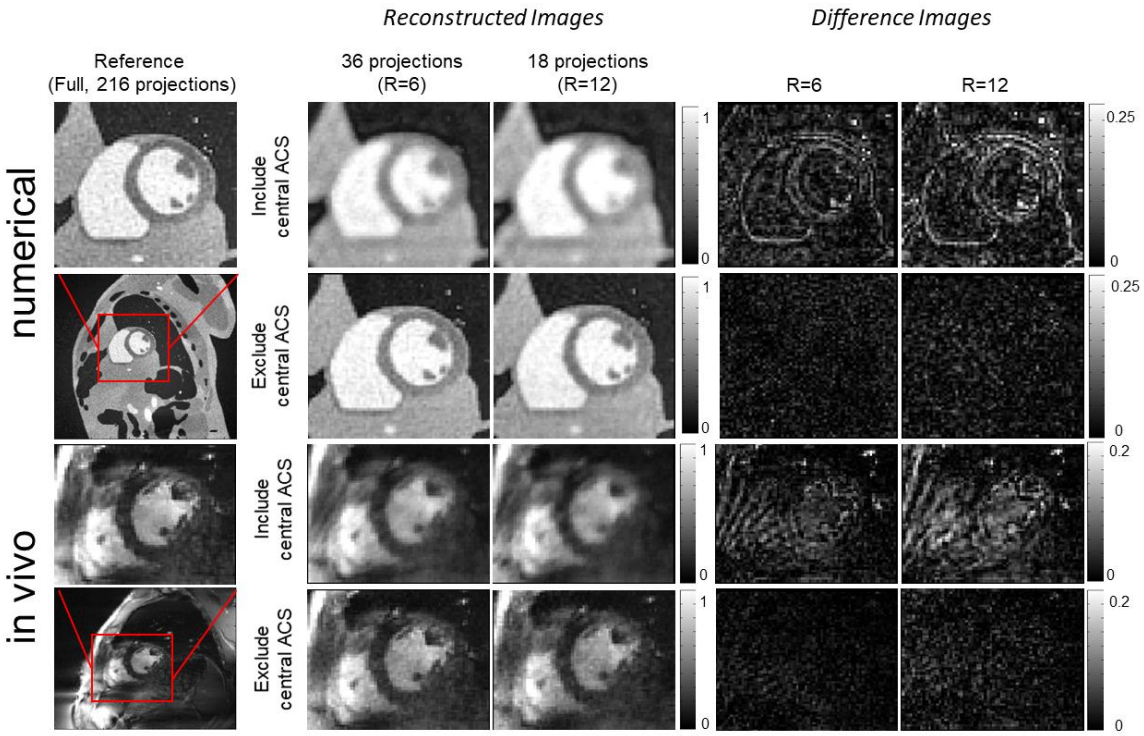

Figure 3: Reconstructed images from SING that include and exclude central ACS data points in numerical simulations (top half) and a cine data set (bottom half) at R = 6 and R = 12. The difference image corresponding to each reconstructed image is shown on the right side of the reconstructed images in the same row.

The radius γ of the excluded central circular ACS region was empirically set to γ= 4 after validating the reconstructed images corresponding to different values of γ of 2, 4, 8, 12, 16. With the inclusion of these central ACS data points in SING calibration, the reconstructed images showed blurring and streaking artifacts at R = 6 and R = 12. By excluding these central ACS data in SING calibration, the reconstructed images demonstrated no visually noticeable blurring or streaking artifacts. For the rest of the SING reconstructions, the central ACS points were excluded from the calibration of each RIK.

3.3.2. Effect of regularization on calibration

Figures 4 and 5 demonstrate the effect of the regularized SING calibration on image reconstructions in numerical simulations and cine imaging, respectively. The signal-based regularization offered visually improved noise performance over the unregularized calibration at R of 6 and 12. At R=6, the signal-based and Tikhonov regularization provided visually similar image sharpness and noise performance. At R = 12, the signal-based regularization offered visually sharper images over Tikhonov regularization.

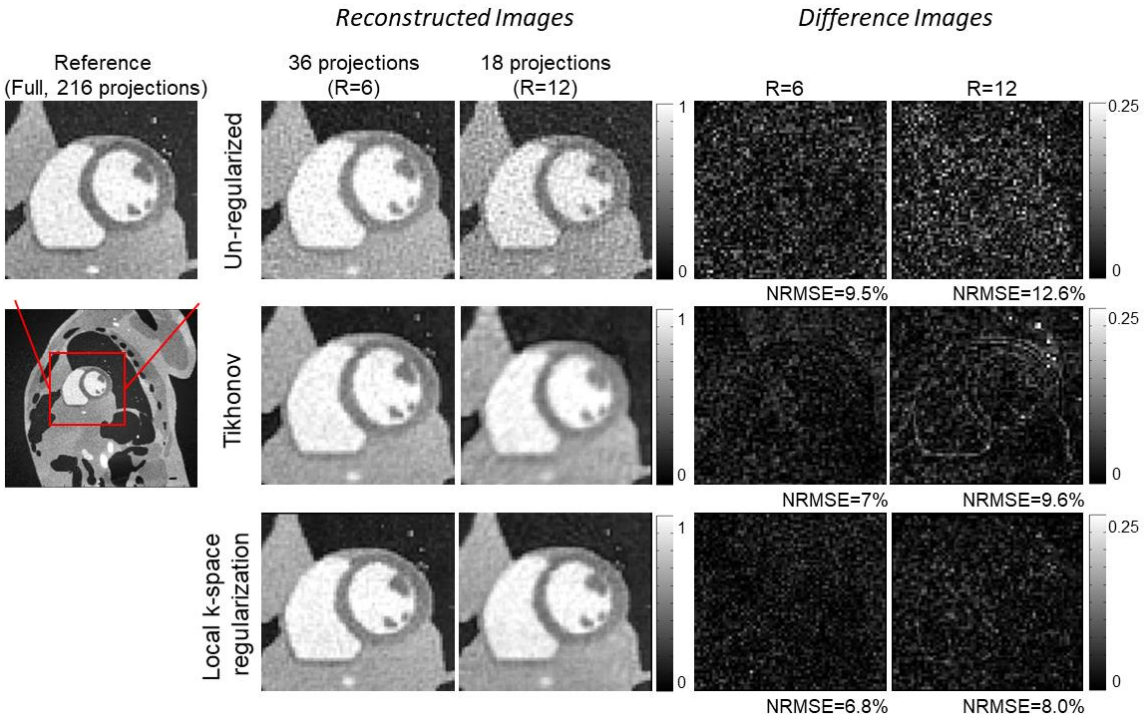

Figure 4: The SING reconstructed images in numerical simulations using unregularized (top row), Tikhonov regularized (middle row), and local k-space regularized (bottom row) RIK calibrations at R of 6 and 12. The difference image corresponding to each reconstructed image is shown at the right side of the reconstructed images in the same row, together with the normalized RMS error (NRMSE) value in the bottom-right side of each difference image.

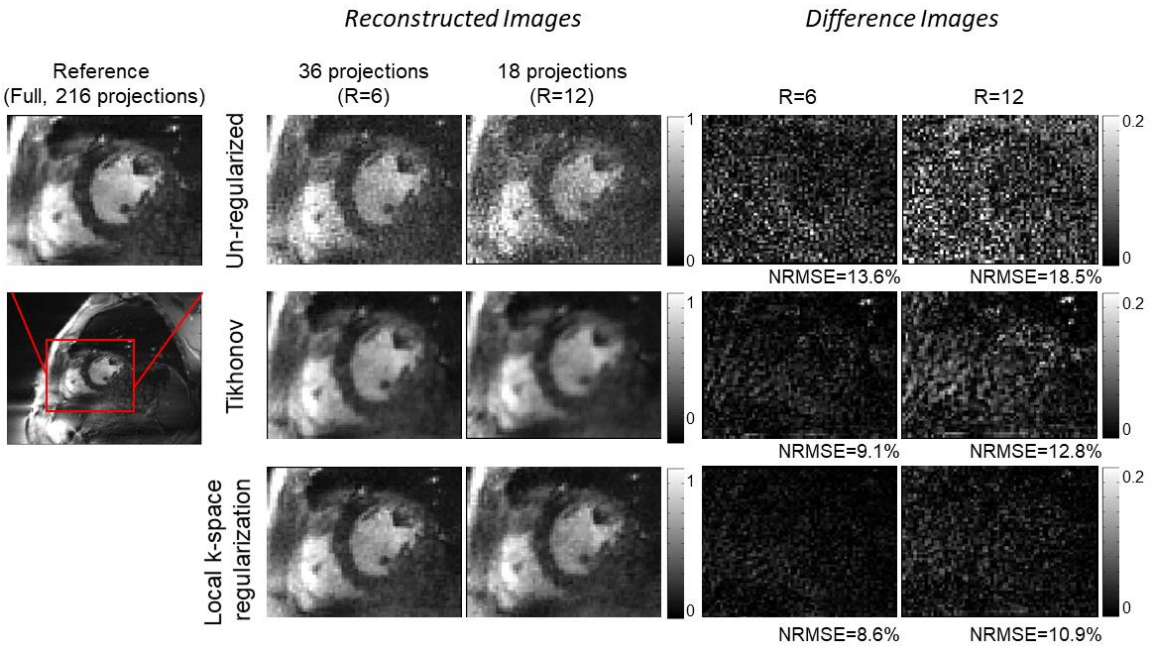

Figure 5: The SING reconstructed images in cine imaging using unregularized (top row), Tikhonov regularized (middle row), and local k-space regularized (bottom row) RIK calibrations at R of 6 and 12. The difference image corresponding to each reconstructed image is shown at the right side of the reconstructed images in the same row, together with the NRMSE value in the bottom-right side of each difference image.

3.3.3. Reconstruction of undersampled acquisitions

Figure 6 shows the results of the numerical simulations with the reconstructions using CG-SENSE, TT-GRAPPA, and SING at R = 6 and R = 12. For R = 6, no visual difference was observed between the TT-GRAPPA and SING reconstructed images, while blurring artifacts were observed in the CG-SENSE image. For R =

12, TT-GRAPPA and SING images were visually similar, whereas the CG-SENSE image showed more blurring and undersampling artifacts.

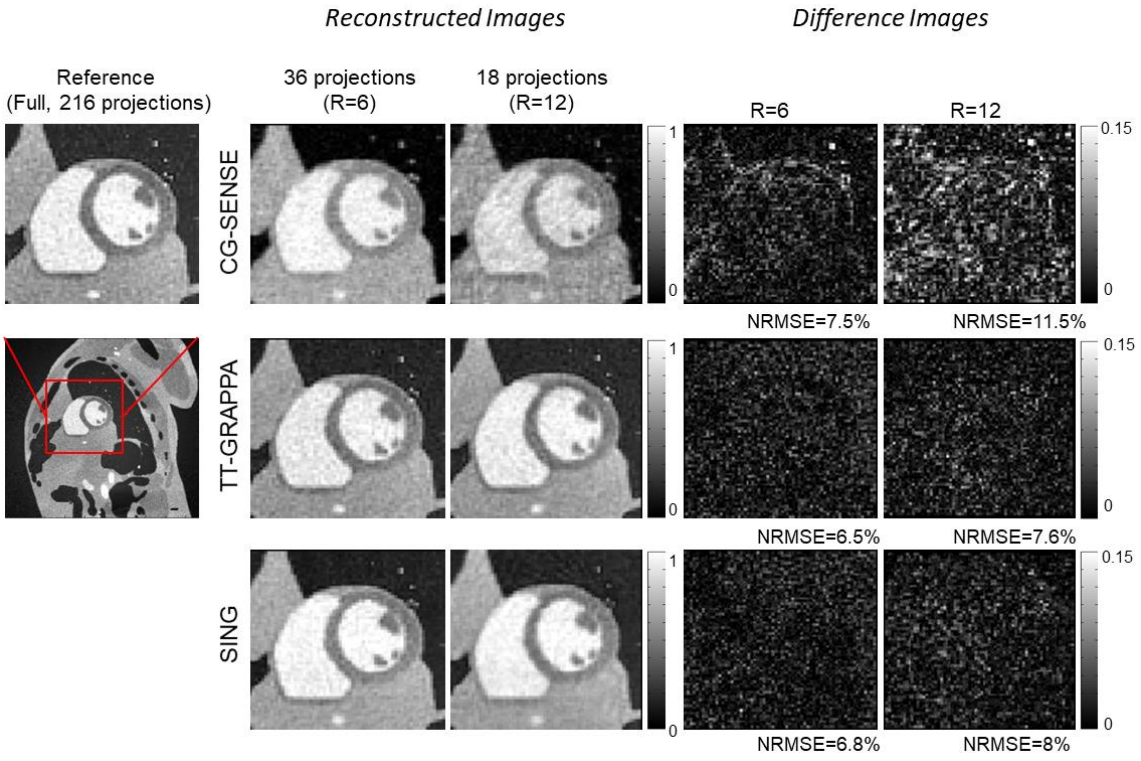

Figure 6: Image reconstructions of radially undersampled data using Tikhonov regularized conjugate-gradient SENSE (CG-SENSE; top row), through-time GRAPPA (TT-GRAPPA; middle row), and SING (bottom row) at R of 6 and 12. The difference image corresponding to each reconstructed image is shown at the right side of the reconstructed images in the same row, together with the NRMSE value in the bottom-right side of each difference image.

Figure 7 shows the reconstruction results from a cine data set using CG-SENSE, TT-GRAPPA, and SING at R of 6 and 12. There was no visual difference among

TT-GRAPPA, SING, and the reference image at R = 6, whereas CG-SENSE resulted in streaking artifacts. At R = 12, there were no visually noticeable blurred or streaking artifacts in TT-GRAPPA and SING images, whereas CG-SENSE yielded to blurred and streaking artifacts. For the other cine data set in which similar results were obtained, normalized RMS error values at R of 6 and 12 were 8.9% and15.3% for CG-SENSE, 8.2% and 10.5% for TT-GRAPPA, and 8.5% and 10.9% for SING.

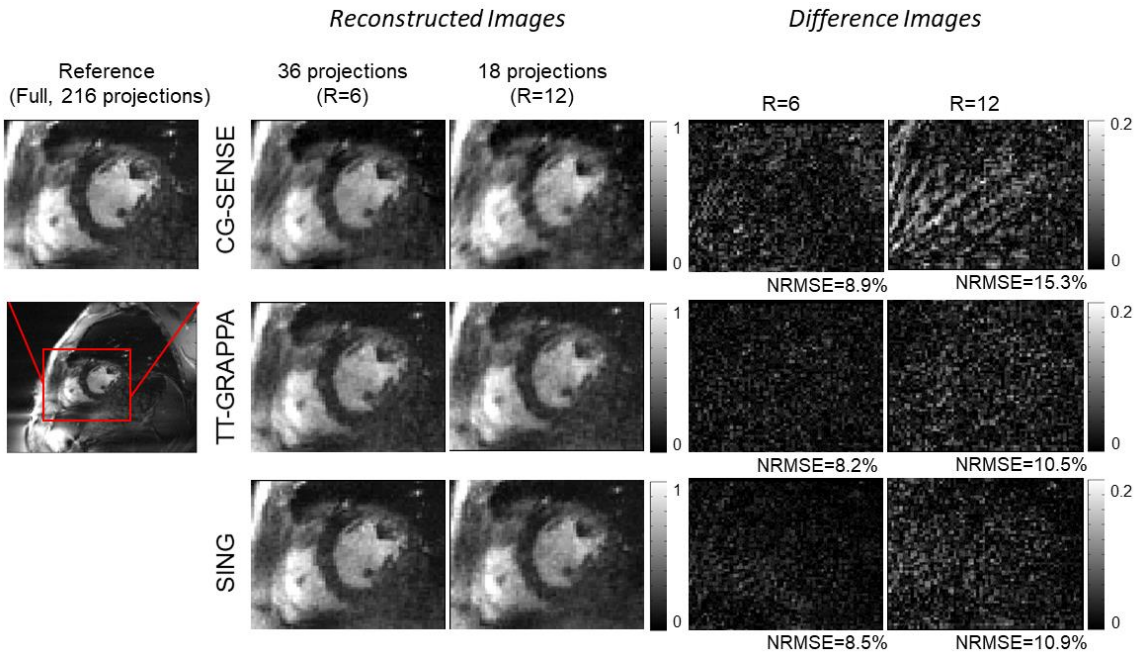

Figure 7: Image reconstructions of the accelerated data in a cine data set using CG-SENSE (top row), TT-GRAPPA (middle row), and SING (bottom row) at R = 6 and R = 12. The difference image corresponding to each reconstructed image is shown at the right side of the reconstructed images in the same row, together with the NRMSE value in the bottom-right side of each difference image.

Figure 8 depicts the temporal intensity profile across the indicated line for CG-SENSE, TT-GRAPPA, and SING. The profiles showed no temporal blurring at R = 6 for TT-GRAPPA and SING, consistent with the absence of any temporal constraints during reconstruction. For CG-SENSE, the profile at R = 6 showed the undersampling artifacts. For R = 12, noise amplifications were observed in the profiles of TT-GRAPPA and SING, whereas the profile of CG-SENSE showed more undersampling artifacts.

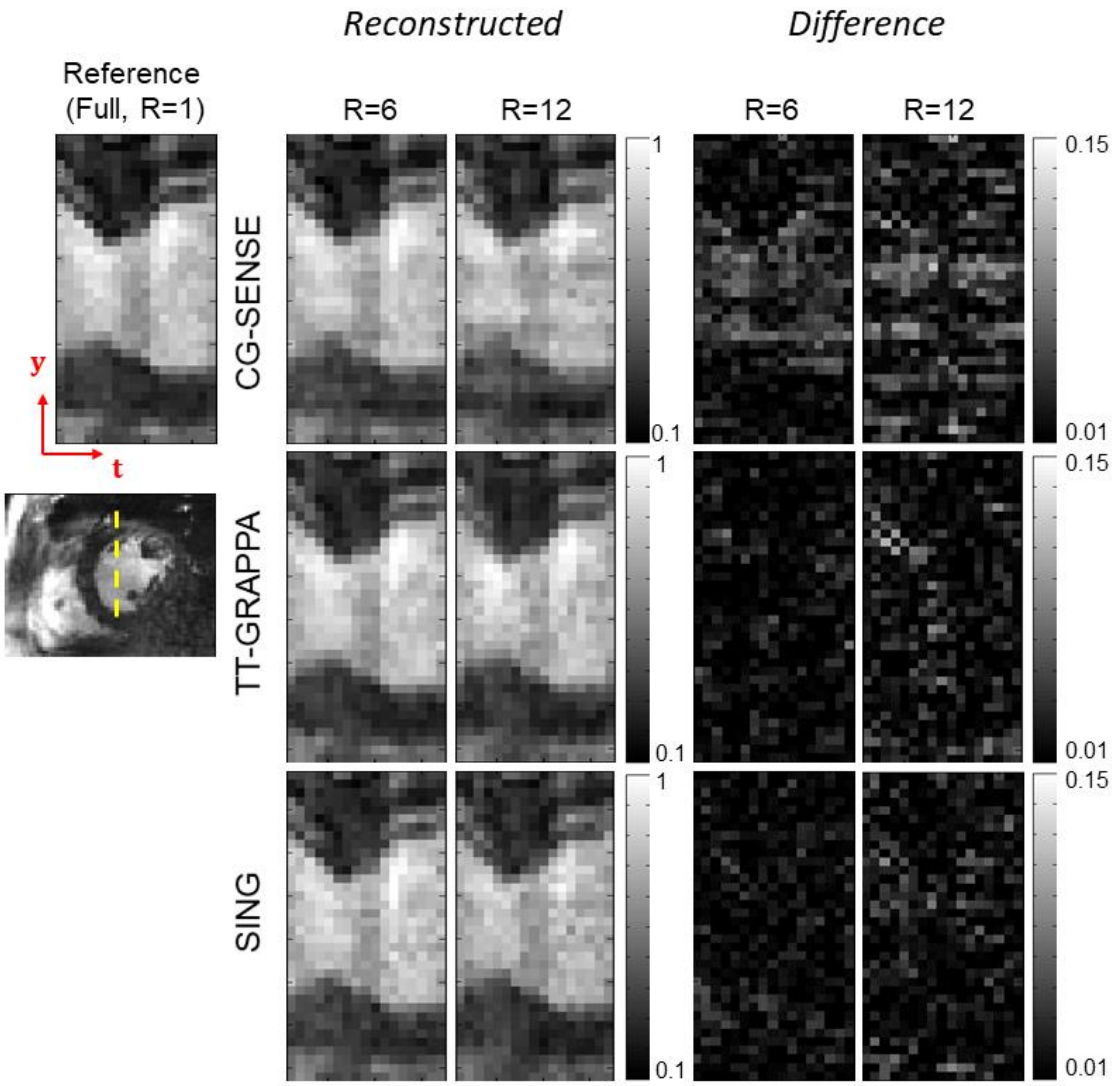

Figure 8: Temporal intensity profiles from 20 cardiac frames across 70 voxels indicated by the yellow line using CG-SENSE (top row), TT-GRAPPA (middle row), and SING (bottom row) at R = 6 and R = 12.

Figure 9 shows g-factor maps of CG-SENSE, TT-GRAPPA, and SING at R = 6 and R = 12. For R = 6 and R = 12, TT-GRAPPA and SING offered similar g-factor over the heart, whereas CG-SENSE yielded higher g-factor than either method. The g-factor maps of TT-GRAPPA and SING were in agreement with the reconstructed images shown in Figure 6, in which either method resulted in similar noisy appearances and normalized RMS error values at R of 6 and 12.

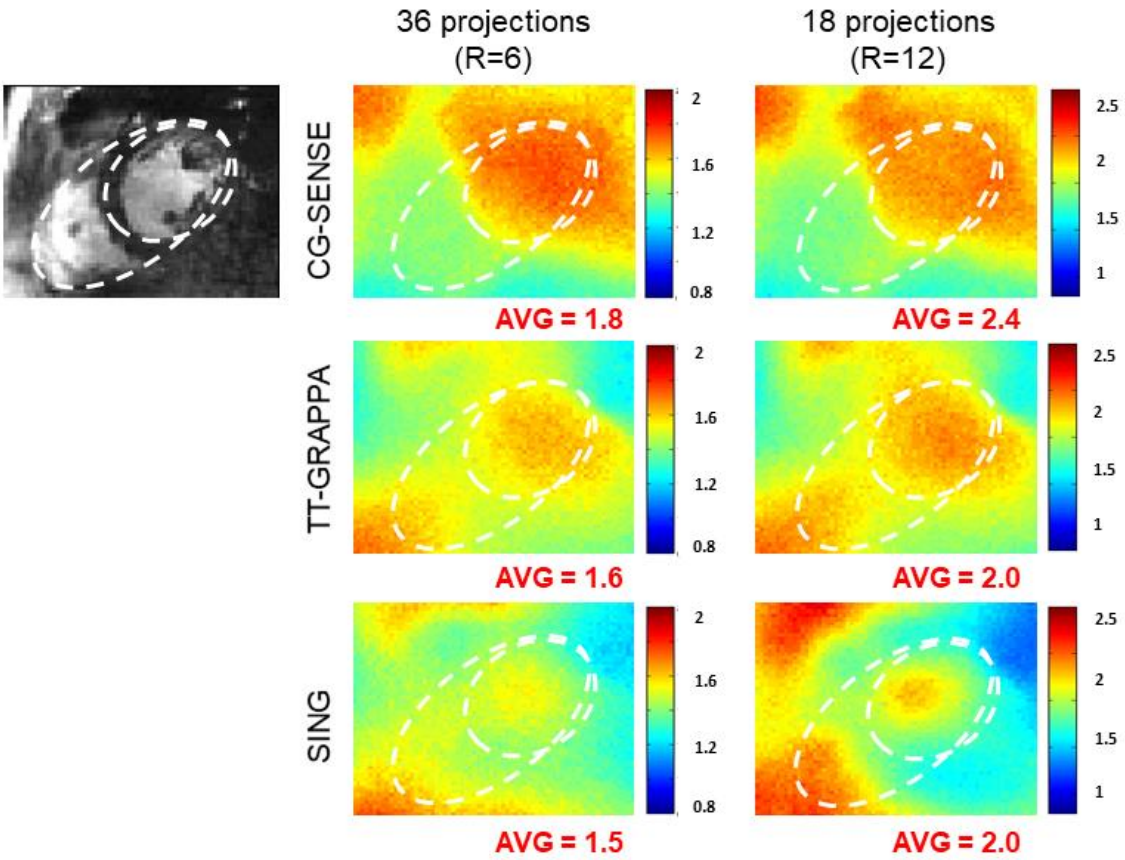

Figure 9: The g-factor maps for CG-SENSE, TT-GRAPPA, and SING reconstructions in the central dashed region at R = 6 and R = 12. The average g-factor value in the same region of each reconstruction was calculated and shown in the bottom-right side of each corresponding g-factor map.

3.4. Discussion

SING enables successful reconstruction of accelerated non-Cartesian acquisitions using self-calibrated RIKs for shortened total imaging time. The reconstruction quality has been shown to be similar to TT-GRAPPA. When using SING, it is sufficient to have a central Nyquist-sampled k-space region to subsequently determine RIKs for undersampled regions of k-space, where calibration data have not been obtained—similar to how Cartesian GRAPPA is typically used with variable density sampling—and benefits dynamic and volumetric imaging. The SING technique requires an additional resampling relative to TT-GRAPPA, but both the gridding and the resampling to the patterns for each RIK can be performed efficiently, with the same computational complexity as TT-GRAPPA. While the convolution-based resampling of ACS data ignores the effect of convolution function, such effect introduces consistent intensity across channels and thus does not have effect on the determination of interpolation kernels.

The exclusion of ACS data at k-space center was found to improve SING reconstructions and was one way to match the quality of the TT-GRAPPA

reconstruction. Previous work on Cartesian GRAPPA[160, 161] found that “outliers,” which have large residuals in a linear calibration system, were from ACS signals at the central k-space region, and the exclusion of central ACS data could improve GRAPPA reconstructions. For SING, the k-space signal intensity is scaled in the proposed regularization approach such that it should be matched in an l_2 sense. The l_2 estimate is a patch measure, and there can still be large variations of the calibration signal in a patch.

Apart from the self-calibration aspect of SING, the proposed local k-space regularization, which adapts to local signal information of the neighboring k-space undersampled data points in the local region of each RIK, is also an important component for improved reconstruction quality. This regularization outperforms Tikhonov regularization with improved sharpness in image reconstruction. By using local SNR levels, the regularization parameters corresponding to each RIK are directly calculated with a scalar division and a scalar multiplication to eliminate alternative computationally intense parameter tuning processes for each RIK. As discussed earlier, such ideas are inherent to TT-GRAPPA, in which the local SNR for the calibration data is the same as the local SNR for the dynamic series. In SING, similar regularization can be maintained for different dynamics, and across different relaxations. The k-space shifting from Luo et al[149] applies equivalent weighting on the signal and noise portion in the measured ACS data, offering an equivalent form of unregularized SING RIK calibration, which was shown to suffer from noise amplification at R = 6 and R = 12.

3D imaging has advantages, such as wider spatial coverage, over 2D imaging. There has been various studies on extending 2D k-space reconstruction to 3D data, including TT-GRAPPA[144, 162] and Arunachalam et al[163], expanding its applicability to 3D imaging studies. In 3D k-space, one extra dimension, relative to 2D, is hypothesized to provide additional signal information. 2D-SING can be a potential candidacy for 3D k-space reconstructions of complicated trajectories including kooshball[164], thanks to its flexibility on arbitrary kernel geometries. In addition, the primary benefit of SING is that its self-calibration strategy can address the challenges of obtaining RIKs with TT-GRAPPA, where lengthy scanning of ACS data is required. The details of extension of 2D-SING to 3D k-space will be provided in the next chapter.

Chapter 4

3D-SING

4.1. Introduction

The reconstructions of accelerated 3D radial (kooshball) trajectories include image based and k-space based methods. CS is a commonly used image-based reconstruction which combines inherent k-space sampling and sparsity of image in an appropriate transform domain to reconstruct image form the accelerated acquisitions. As an alternative k-space reconstruction, radial GRAPPA first extended GRAPPA to non-Cartesian imaging and proposed angular-invariant/readout-variant interpolation kernels to reconstruct undersampled radial data[23]. The region-specific interpolation kernels (RIKs), later proposed in through-time radial GRAPPA (TT-GRAPPA[24]), significantly improved the reconstruction quality of radial undersampling, but necessitated additional calibration scans. As a result, obtaining RIKs for 3D TT-GRAPPA is challenging due to the long calibration scanning, thereby limiting in general the use of k-space methods for 3D non-Cartesian imaging. Our early method AIM proposed to generate ACS data without additional calibration scans to self-calibrate RIKs with potential scalability to 3D data. Later, Luo et al[149] has demonstrated self-calibrated a non-Cartesian 2D/3D GRAPPA method by calibrating different RIKs on a central Cartesian ACS region without additional calibration data, and the reconstruction quality was shown to be

similar to Conjugate Gradient SENSE (CG-SENSE) on stack-of-stars and 2D radial datasets.

This chapter introduces 3D-SING for kooshball imaging to address the challenges of calibrating RIKs when additional ACS data is not available, as well as to improve reconstruction quality. The 3D-SING reconstruction is evaluated on 3D coronary MRI and compared to gridding, CG-SENSE, and CS reconstruction methods.

4.2. Method

4.2.1. Self-calibration of 3D RIKs for kooshball acquisitions

3D-SING interpolation using a RIK in a local k-space region for multi-channel acquisitions is represented as:

$$s_j(\mathbf{k}) = \sum_{i=1}^{N_c} \sum_{\Delta\mathbf{k}\in\Omega} w(i, j, \mathbf{k}, \Delta\mathbf{k}) \cdot s_i(\mathbf{k} + \Delta\mathbf{k}), \tag{6}$$

where $s_j(\mathbf{k})$ represents a missing point at the k-space coordinate denoted by the vector $\mathbf{k}$ in jth channel (j=1,2,..N_c, and N_c is the number of channels), $s_i(\mathbf{k} + \Delta\mathbf{k})$ denotes a neighboring acquired point in ith channel at the k-space coordinate represented by the displacement vector $\Delta\mathbf{k}$ with respect to the missing location $\mathbf{k}$. The set Ω includes the displacement vectors, with respect to the missing coordinate $\mathbf{k}$ for surrounding acquired points. The RIK, $w(i, j, \mathbf{k}, \Delta\mathbf{k})$ is unique for the location of $\mathbf{k}$ and $\Delta\mathbf{k} \in \Omega$.

3D-SING's flow chart of the self-calibration of RIKs is illustrated in Figure 10.

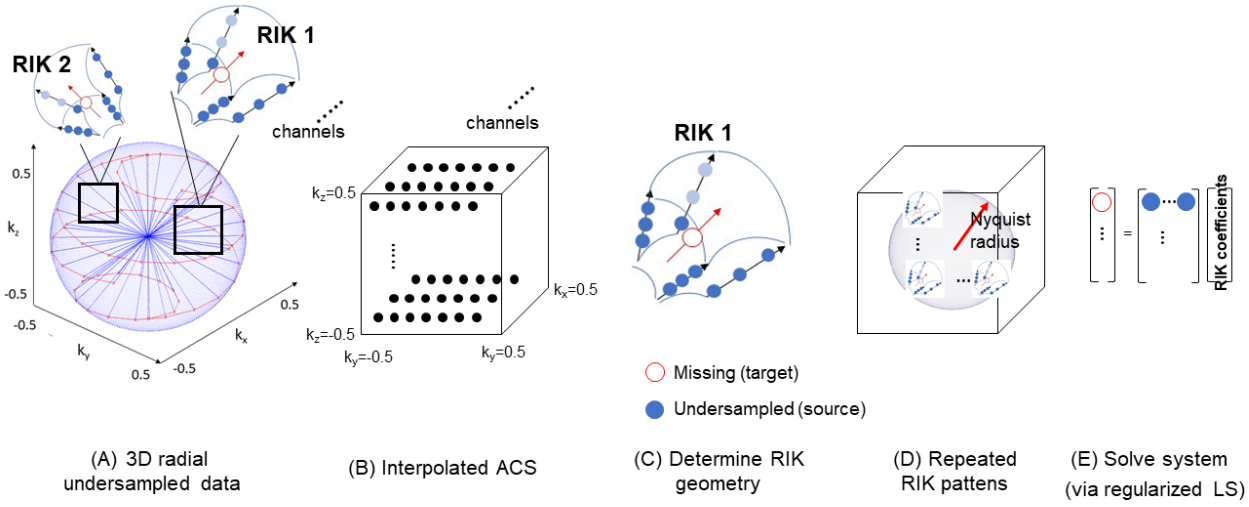

Figure 10: The SING schematic of calibrating a RIK using the undersampled radial data (**A**). The ACS data on Cartesian grid is generated from the interpolation of the undersampled radial data (**B**). Repeated sampling patterns with a distinct RIK geometry are synthesized from the interpolation of the ACS data (**D**). Those patterns form a linear calibration system which is then solved via regularized least-squares to obtain the coefficients of the RIK. The calibration of different RIK is performed by repeating (C)-(E).

The acquired k-space that is used for calibration is linearly interpolated to a 3D Cartesian grid whose central part, a Nyquist rate sampled ACS region, is then used to calibrate different RIKs. The patterns of acquired and missing locations, which are denoted by $\mathbf{k} + \Delta\mathbf{k}$ and $\mathbf{k}$ for $\Delta\mathbf{k} \in \Omega$ respectively, are generated repeatedly in the ACS region via linear interpolation of the ACS data and used to calibrate the RIK. The estimated RIK is convolved with the surrounding undersampled data to

interpolate missing measurements in the region of undersampled k-space. Different RIKs are obtained for distinct patterns until the missing k-space is reconstructed.

The ACS data (Figure 10B) are computationally generated via linear interpolation of the undersampled kooshball data (Figure 9A) in each coil. For a RIK, its geometry (Figure 10C) is determined by the k-space coordinates of the missing point (referred to as target point) and its neighboring sampled points (referred to as source points). Once the RIK geometry is specified, the shift-invariance property of convolution is utilized to generate the repeated patterns of the RIK (Figure 10D) via convolving the ACS data $\mathrm{A_i}(\mathbf{k})$ and the Kaiser-Bessel kernel. These repeated patterns establish an overdetermined linear system with GRAPPA source and target formulation for calculating the RIK. The overdetermined level of the system can be characterized by the ratio v of the number of the synthesized repeated patterns N_p and the number of coefficients of the RIK $N_{RIK} = N_c \cdot |\Omega|$, that is $v = \frac{N_p}{N_{RIK}}$, where $|\Omega|$ is the cardinality of Ω. For the kooshball acquisitions (the total number of projections is denoted by N_{proj}) all repeated patterns inside the Nyquist radius, $r_{Nyq} = \sqrt{N_{proj}/2\pi}$, and not inside a central sphere with radius $4\Delta k$ are used. Each of the repeated patterns is shifted relative to one another along three directions of the k-space by $2\Delta\mathrm{k}$, corresponding to the width of Kaiser-Bessel resampling window. The linear system is solved via regularized least-squares where regularization matrices are added to the calibration system to match the SNR of the ACS data and the undersampled data. Similar to our previous 2D-SING[165], the RIK coefficients are obtained from

$$\min_{\mathbf{w}} \|(\mathbf{b} + \Delta\mathbf{b}) - (\mathbf{G} + \Delta\mathbf{G}) \cdot \mathbf{w}\|_2^2, \quad (7)$$

where $\mathbf{b}$ is a vector of target points of size M×1, $\mathbf{G}$ is a matrix of source points of size M×N_{RIK}, $\mathbf{w}$ is a vector with size N_{RIK}×1, and the regularization terms $\Delta\mathbf{b}$ and $\Delta\mathbf{G}$ are complex valued noise matrices with matched dimensions. The regularization matrices $\Delta\mathbf{b}$ and $\Delta\mathbf{G}$ are calculated as $\Delta\mathbf{b} = \mathbf{D} \cdot \boldsymbol{\chi}$ and $\Delta\mathbf{G} = \mathbf{D} \cdot \mathbf{X}$, respectively, where $\mathbf{D}$ is a diagonal matrix with d_m the mth diagonal entry and the elements of $\boldsymbol{\chi}$ and $\mathbf{X}$ complex valued standard normal distributed. The mth entry in $\mathbf{D}$ is calculated as $\mathrm{d}_m = \sigma \cdot \mathrm{a}_m / u$, where σ is the standard deviation of the thermal noise, a_m is the l_2 norm of the mth row of the matrix $\mathbf{G}$, and u is the l_2 norm of the undersampled points where the RIK is applied.

A missing k-space point is reconstructed using Eq. (6) with the calculated RIK. The calibration and application of other RIKs are repeated until all missing samples are reconstructed. The reconstructed k-space data is then transformed to image space via gridding to obtain reconstructed image of each channel. Each coil image is weighted by the conjugate of the coil map and summed across the coil dimension to obtain the final reconstructed image[166, 167].

4.2.2. Implementation details of 3D RIKs

$N_{RIK} = N_c \cdot |\Omega|$ determines the size of a RIK, where $|\Omega| = \mathrm{n}_v$×n_r for the kooshball acquisition with n_v and n_r denoting the source projections and the points along projections used. The latter are selected as the $\pm\frac{\mathrm{n}_r - 1}{2}$ readout samples of the

source projections. For the kooshball acquisition, the kernel size of each RIK 4×5 $(\mathrm{n}_v \times \mathrm{n}_r)$ is used.

Locally shift-invariant RIKs along the readout direction, due to similar sampling patterns in the neighborhood of each missing k-space point, enables the reduction of the number of different RIKs needed for the full k-space reconstruction. In this paper, similar to TT-GRAPPA and to improve computational efficiency, a single RIK is used as a shift-invariant interpolation kernel for the interpolations of 8 neighboring readout samples ($\pm 2\Delta\mathbf{k}$) on the same projection.

4.2.3. Whole-heart coronary MRI datasets

3D whole-heart coronary MRI data were acquired at Lausanne University Hospital, Lausanne, Switzerland. All participants provided written informed consent and the study was approved by the local institutional review board. Nine participants were scanned on a 1.5T clinical scanner (MAGNETOM Aera, Siemens Healthcare, Erlangen, Germany). The acquisition protocol was a prototype 3D radial ECG triggered T_2-prepared, fat-saturated, navigator-gated bSSFP imaging sequence with TR/TE=3.0/1.56ms, flip angle=115°, voxel size=$(1.15\text{mm})^3$, base matrix=384^3, FOV=$(440\text{mm})^3$, with 2-fold readout oversampling. 12320 radial projections (sub-Nyquist rate of 5) were acquired in 385 heartbeats with the spiral phyllotaxis pattern[168] using an imaging window of 96ms per heartbeat or equivalently 32 projections per interleaf. A diaphragmatic respiratory navigator was used for gating

the respiratory motion with a 5mm gating window[169]. The number of coil elements used for signal reception were 26, 30, 20 and 30 for the nine subjects respectively.

4.2.4. Reconstruction experiments

3D kooshball coronary MRI data were retrospectively uniformly undersampled between interleaves for four acceleration rates (R) of 3, 4, 5, 6. The evaluated reconstruction methods include 3D-SING, gridding, CG-SENSE, and CS.

The implementation of gridding reconstruction followed Jackson et al[169]. The channel combination was implemented as the summation of coil images weighted by the conjugate of the coil map across the coil dimension to compute the final gridding image[166, 167]. The CG-SENSE reconstruction was implemented as in Pruessmann et al[22] for iteratively solving the optimization problem $\min_{\mathbf{x}}\|\mathbf{y}-\mathbf{E}\mathbf{x}\|_2^2$ using conjugate gradient with preconditioner. The stopping criterion was implemented to minimize the relative l_2 norm difference between two subsequent iteration images to less than 1%. The final image was empirically selected after the visual inspections on the last ten images.

The CS reconstruction used the objective function

$$\min_{\mathbf{x}}\|\mathbf{y}-\mathbf{E}\mathbf{x}\|_2^2+\lambda\Psi(\mathbf{x}), \tag{8}$$

where $\mathbf{y}$ denotes the undersampled data in all channels, $\mathbf{E}$ is the SENSE encoding matrix, $\mathbf{x}$ is the reconstructed image, and Ψ is the 3D spatial Total Variation (TV)[9]. This was solved using alternating direction method of multipliers (ADMM)[96]. The

TV parameter λ was empirically set to 1/50 of the maximum absolute value of the gridding reconstruction of the undersampled data, and the penalty parameter in the ADMM procedure was set to 0.5[96]. The details of the empirical selection of these two CS parameters are provided in the Appendix A. The stopping criterion using the relative l_2 norm difference between two subsequent iteration images was set to be smaller than 0.01.

4.2.5. Image analysis

Quantitative image assessments of the retrospectively undersampled acquisitions are performed using the Normalized Root Mean Square Error (NRMSE) and Structural Similarity index[170] (SSIM) with respect to the reference image, defined as the gridding reconstruction of all available measurements. The NRMSE and SSIM are computed over a three-dimensional volume-of-interest that covers the whole heart.

Additionally, automated reference-free image quality assessment was performed with a recently reported deep convolutional neural network for image quality assessment (IQ-DCNN)[171]. The IQ-DCNN was already trained to mimic human expert visual assessment of 3D radial whole-heart coronary MR images. The different methods and acceleration rates were anonymized and randomized for the blinded assessment of reconstructions quality. For each reconstruction and acceleration rate, the IQ-DCNN provided an image quality score in the continuous range 0 (nondiagnostic) to 4 (excellent diagnostic value).

4.3. Results

Figure 11 shows the cropped axial slices from a 3D coronary MRI dataset reconstructed using gridding, CG-SENSE, CS and 3D-SING reconstructions across the retrospective acceleration rates of 3, 4, 5, and 6. The gridding reconstruction of all measurements is used as the reference image. The gridding reconstructions at higher acceleration rates suffer from streaking artifacts due to excessive undersampling, which lead to degradation of image quality as the acceleration rate is increased. CG-SENSE has visible noise amplification, which appears stronger as the rate increases. For CS, the noise amplification across all acceleration rates is less prominent than CG-SENSE, but blurring artifacts are observed relative to gridding and CG-SENSE. Compared with CS, 3D-SING has lower visible blurring across all rates. Additionally, 3D-SING has less visible noise amplification than CG-SENSE, and less pronounced undersampling artifacts than gridding at all rates. The visual degradation of image quality for higher acceleration rates with respect to the reference image is noticeable across all methods, though it is less severe for 3D-SING.

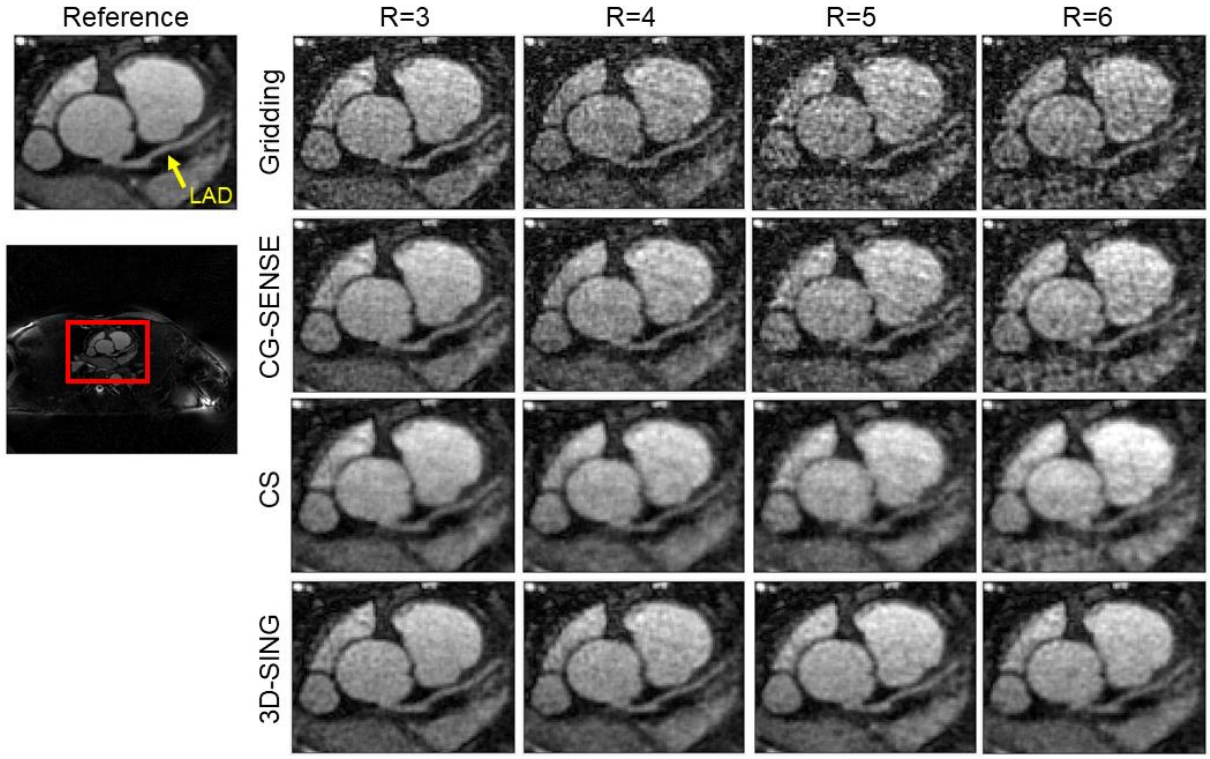

Figure 11: The cropped axial slices from a 3D coronary MRI dataset reconstructed with gridding, CG-SENSE, CS, and 3D-SING at retrospective rates of 3, 4, 5, and 6. The reference image, gridding reconstruction of all projections, is shown in the left column for the gridded FOV of $(440mm)^3$ from the data acquired with a nominal $(220mm)^3$ FOV. The cropped region has a FOV of $80\times103mm^2$. LAD=Left Anterior Descending artery.

Figure 12 shows the reformatted coronal images using the SoapBubble[172] tool, from a different subject, reconstructed with gridding, CG-SENSE, CS, and 3D-SING. For gridding, the RCA and LCX are visible at rates 3, 4 and 5, but with artifacts. At rate 6, a shorter LCX is observed in gridding. For CG-SENSE, the RCA and LCX are also visible at rates of 3, 4, and 5, but degraded relative to the

reference due to noise amplification. At rate 6, a shorter LCX is seen in CG-SENSE. Likewise, for CS, the RCA and LCX are visible at all rates, but has blurring artifacts. 3D-SING provides improved visualization of the RCA and LCX across all rates.

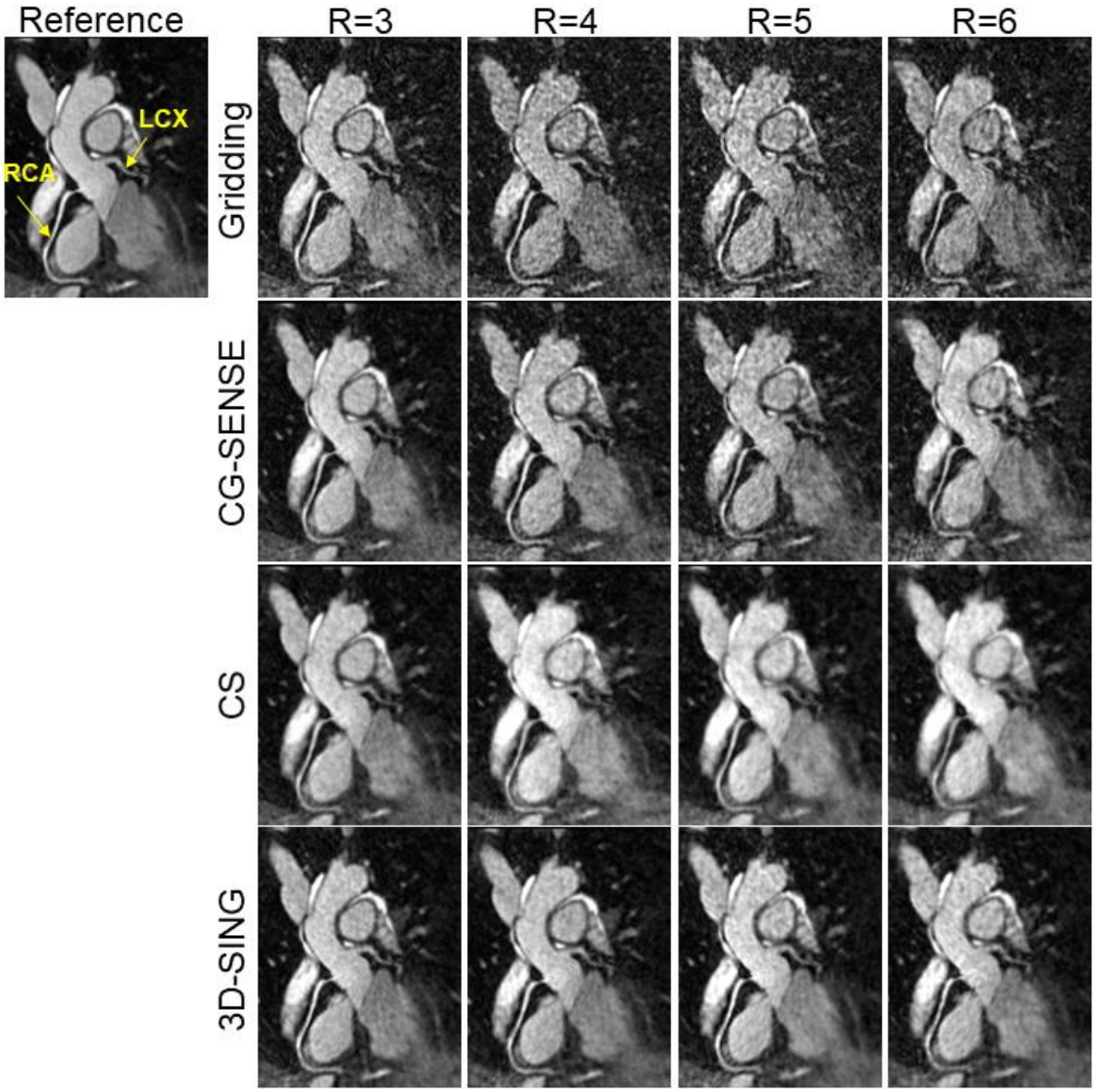

Figure 12: The reformatted coronal images in the cropped region, of a 3D coronary MRI dataset from a different subject, reconstructed with Gridding, CG-SENSE, CS and 3D-SING at retrospective rates 3, 4, 5, and 6. The reference, which is the

reformatted gridding reconstruction of all the acquired projections, is shown in the left column. RCA= right coronary artery, LCX= left circumflex.

The NRMSE and SSIM values across all subjects are shown in Figure 13. Compared to other methods, 3D-SING has consistently the lowest mean value of NRMSE and the highest mean value of SSIM across the rates of 3, 4, 5, and 6. At rate 3, CG-SENSE and CS have similar quantitative quality evaluated with NRMSE and SSIM, while 3D-SING has improved quantitative performance.

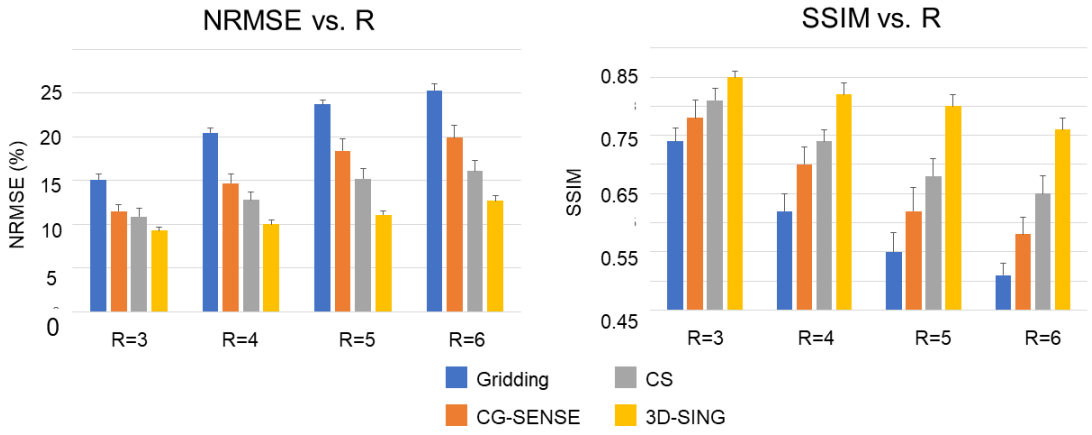

Figure 13: The NRMSE and SSIM, from nine subjects, are shown as mean±standard deviation for each of the reconstruction methods at four different accelerations.

Figure 14 shows the image quality assessment (IQA) scores across all subjects computed using the reference-free deep learning method for different methods at the four acceleration rates. 3D-SING has consistently highest mean value of IQA

score compared to other methods at all rates, while they are all lower than the mean score of the reference image. At rate 3, CG-SENSE and CS have similar mean values of IQA scores, while 3D-SING has higher mean score than the two methods. For rates larger than 3, the spread in score between CG-SENSE and CS increases with CS performing better, in parallel the spread in scores between 3D-SING and CS increase with 3D-SING performing better, and 3D-SING for R=6 being similar to CS with R=3 for the IQA score.

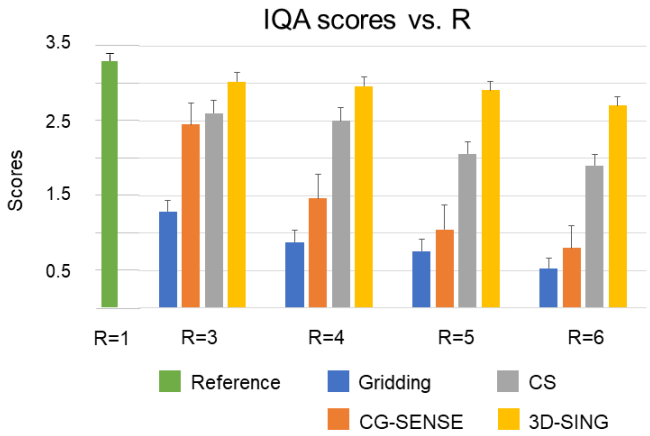

Figure 14: The imaging quality assessment scores, shown as mean±standard deviation, are calculated from nine subjects using a reference-free deep learning method for different methods at rates 3, 4, 5, and 6. The score of the reference image is included.

4.4. Discussion

Chapter 3 introduced 3D-SING, a non-iterative non-Cartesian parallel imaging technique, for 3D k-space reconstruction and demonstrated its efficacy on

kooshball coronary MRI. RIKs of 3D-SING were self-calibrated form undersampled data without additional acquisitions of multiple calibration scans, thereby reducing total imaging time. The use of the self-calibrated RIKs in 3D-SING enables successful reconstructions of accelerated kooshball acquisitions, as evidenced by both its quantitative and qualitative evaluations with respect to gridding, CG-SENSE, and CS.

The RIKs in TT-GRAPPA, calculated from multiple calibration acquisitions, have been shown to provide superior reconstruction quality compared with CG-SENSE in 2D radial imaging. The reconstruction quality of TT-GRAPPA was matched by 2D-SING using adaptive regularization for the calibration of each RIK. The regularization in 3D-SING, by adding $\Delta\mathbf{b}$ and $\mathbf{G}$ in Equation (7), generates a RIK which enables simultaneous balance between the contributions of the spatially-variant signal and the spatially-invariant noise in the k-space interpolation. No tuning of parameter is required in the regularization of 3D-SING. The regularization matrices are additive to the measurements, thereby leading to minimal effect on the computation time for calculating the RIKs.

The Nyquist sampled ACS data, which is used for the estimation of sensitivity profiles in CG-SENSE and CS and the calibration of RIKs in 3D-SING, is reduced as the acceleration rate R is increased. A separate fully sampled low-resolution acquisition enables the estimation of the sensitivity profiles for CG-SENSE and CS, and similarly can enable the calibration of RIKs on 2D/3D non-Cartesian imaging. Using a separate acquisition to increase feasible acceleration rates with 3D-SING warrants further investigation.

Vessel sharpness is a referenceless quality measure for coronary MRI[132-134, 173-179]. However, not all reconstruction methods enable clear visualization of the coronary arteries at high acceleration rates due to noise and other artifacts, especially in the middle and distal regions. Thus, it is difficult to track the vessels with the sharpness measurement algorithm. Instead, we used an AI-based IQA algorithm to evaluate different reconstruction methods. This method previously demonstrated utility in quality comparisons between images at different iterations in a CS algorithm. It offers a relative ranking between the performances of different reconstruction methods, which was consistent with the visibility of artifacts.

The continuous resampling of ACS data in SING enables the estimation of arbitrary shape of kernel geometry, leading to potential feasibility of k-space based interpolation for the sophisticated three-dimensional sampling trajectories such as 3D shells[180], 3D cones[181], spherical stack of spirals[182], and 3D distributed spirals[183], which warrant further investigation. In addition, 3D-SING could be applied to free-breathing motion-corrected whole-heart MRA. A recently developed SIMBA technique[184], which aims to find a motion-consistent subset, could be combined with 3D-SING to reconstruct a full motion-resolved k-space.

2D dynamic cine imaging and 3D anatomical coronary whole-heart imaging have been investigated for the applicability of the 2D-/3D-SING method. While the k-space reconstructions for 3D imaging has been shown on perfusion[144] and angiography[142] studies, its applicability on DCE prostate imaging has not been demonstrated yet. The next chapter will show the efficacy of 3D-SING on DCE prostate imaging.

Chapter 5

Dynamic Contrast Enhanced (DCE)-MRI imaging

5.1. Introduction

The k-space reconstruction methods (GRAPPA) for non-Cartesian data are suited for various MRI imaging applications[24, 26-28]. Cardiac MRI is a primary application that SING is evaluated with in chapter 3 and 4. In this chapter, SING is assessed using DCE-MRI data.

T1-weighted dynamic contrast enhanced (DCE)-MRI is a valuable and still evolving technique for mapping of the spatial distribution of body vascular parameters such as perfusion, permeability, and blood volume[186, 187]. Series of T1-weighted images are acquired before, during, and after a bolus injection of a gadolinium-based contrast agent (CA). The changes in the CA concentration are derived from the changes in the signal intensity and then regressed to quantify pharmacokinetic parameters[79, 188]. DCE-MRI has been used for quantitative assessment of brain tumors[73, 189, 190], multiple sclerosis lesions[191], Alzheimer's disease[192], and other neurological disorders with blood-brain barrier disruption. DCE-MRI is also utilized in clinical oncologic imaging for the assessment of breast[193] and prostate cancer[194].

While its usefulness has been demonstrated, the conventional clinical DCE-MRI is limited by low spatial/temporal resolution and insufficient spatial coverage. Low temporal resolution also results in poor reproducibility of pharmacokinetic parameters[195, 196]. A typical clinical DCE scanning provides 2-30s temporal resolution for the detection of signal intensity changes which result from contrast agent perfusion[186]. As a result, the in-plane voxel dimensions usually exceed $1mm^2$ and the thickness of slice is often greater than 5 mm thick. Such spatial resolution is often inadequate to cover the known pathology.

CS theory has inspired a wide array of new data acquisition and constrained reconstruction strategies that aim to reconstruct images from sparsely undersampled data[8]. As mentioned earlier in the thesis, CS is well suited for dynamic imaging, in which redundancy of information can be exploited in the temporal dimension, using dictionary learning[197, 198] or high-pass filtering[88, 90]. The combination of parallel imaging and CS has been shown to greatly accelerate the data acquisition, while achieving significantly higher spatiotemporal resolution and large spatial coverage with only slight image quality penalties[29, 97, 158]. Several groups have also utilized undersampling and constrained reconstruction methods to accelerate contrast-enhanced magnetic resonance angiography (MRA). CE-MRA is particularly amendable to this reconstruction strategy because subtraction angiograms are sparse in the image domain. High spatiotemporal resolution and broad coverage are achieved by exploiting high image contrast and a high degree of image domain sparsity. Barger et al.[199] used undersampled 3D projection reconstruction trajectories and a view-sharing scheme to achieve isotropic

resolution and 4s temporal resolution. Haider et al.[200] used a Cartesian radial hybrid technique in combination with 2D SENSE, partial Fourier, and view-sharing to achieve 1-2 mm isotropic resolution and subsecond temporal resolution.

The k-space based reconstruction, alternative to CS, can also accelerate scans in dynamic imaging. A fully-sampled separate ACS dataset is required to estimate interpolation kernels for reconstruction. When a time-interleave sampling scheme, adjacent time frames can be merged to build a fully-sampled ACS dataset, while eliminating the need for separate ACS data. Breuer et al.[84] proposed TGRAPPA method to calibrate the kernel weights using only the acquired data in dynamic cardiac imaging with time interleaved sampling. Arunachalam et al.[163] extended the time-interleave sampling scheme to radial trajectories for radial GRAPPA reconstruction. The angular-invariant/readout-variant interpolation kernels were used. Seiberlich et al.[24] later demonstrated that RIKs outperform such kernels in reconstruction quality. In a subsequent study[142], the authors suggested the use of RIKs on 3D MR angiography. However, additional ACS data is required to calibrate RIKs, thereby limiting its applications when separate acquisitions of ACS data are not available.

The self-calibration approach for the calibration of RIKs can be exploited to address the challenge of k-space reconstruction when additional ACS data are not acquired. Luo et al.[149] has shown their use on reconstruction of 3D stack-of-stars trajectories for static imaging application. The reconstruction using self-calibrated RIKs on stack-of-stars trajectories for DCE imaging, which to our knowledge has not been demonstrated, is the main topic in this chapter.

5.2. Methods

5.2.1. Self-calibration of RIKs on stack-of-stars sampling

The self-calibration of RIKs in SING used Cartesian ACS data to calibrate each RIK, whose flowchart was illustrated in Figure 15.

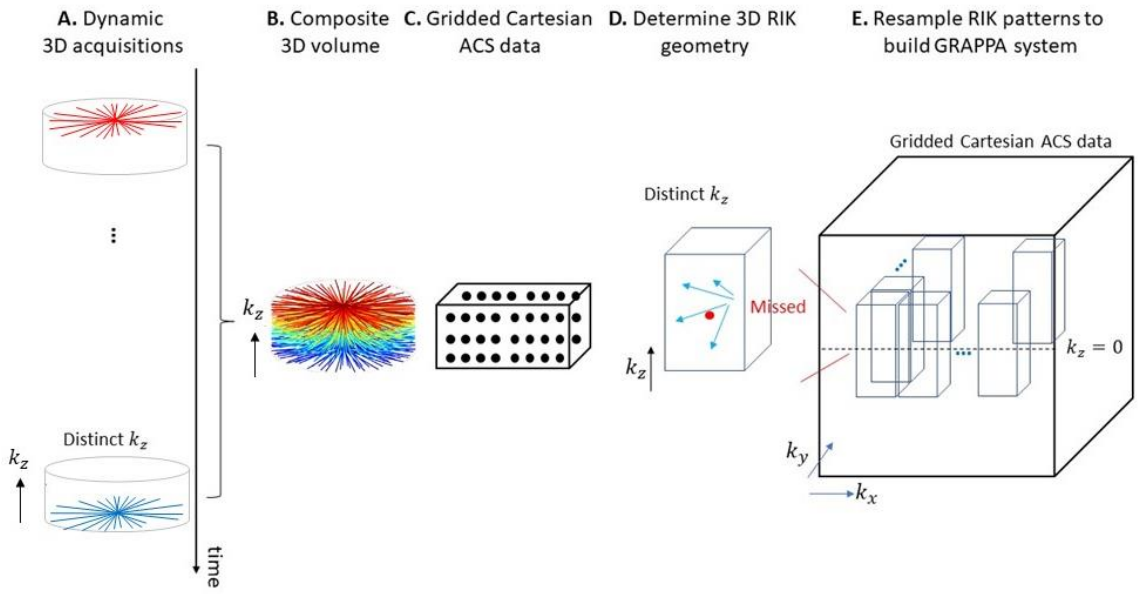

Figure 15: The flowchart of resampling repeated RIK patterns.

First, the dynamic data, whose sampling patterns were interleaved stack-of-stars trajectories through time, were combined into a single fully-sampled 3D composite volumetric dataset. Subsequently, the Kaiser-Bessel convolution was performed on the composite dataset and resampled on a Cartesian grid to generate 3D ACS data. The ACS region, which was empirically to be three central k_z planes, is then

used to calibrate RIKs. The Cartesian points in the ACS region were convolved with a Kaiser-Bessel window with width Δk (Δk: Nyquist interval) to resample repeated patterns of each RIK. These RIK patterns build a linear overdetermined system and solving the system via regularized least-squares obtains the kernel weights of the RIK.

To regularize the calibration of RIKs for stack-of-stars sampling, noise matrices are added to both target vector and source matrix in the linear system, similar to the RIK calibrations for 2D and 3D radial imaging. The added noise matrices enabled matched SNR between ACS data and undersampled data.

5.2.2. Implementation details of RIKs on stack-of-stars sampling

One important RIK feature, which determines the quality of reconstruction, is its size. The kernel size is $n_v \times n_r$, where n_v and n_r represent the number of source projections and readouts near each missing point. The n_v source projections are selected as the nearest ones to each missing spoke, and the n_r source readouts are selected as $\pm(n_r - 1)/2$ readout samples relative to each missing readout. For the reconstruction of stack-of-stars data, the kernel size of each RIK 4×5 $(\mathrm{n}_v \times \mathrm{n}_r)$ is used.

Similar sampling patterns in the neighborhood of each missing k-space point lead to local shift-invariance of RIKs along the readout direction, thereby enabling the reduction of the number of different RIKs for full k-space reconstruction. A single RIK is used as a shift-invariant kernel along the readout direction in order to

improve computation efficiency. In the DCE study, one RIK is utilized for the reconstructions of 8 adjacent readout samples across $\pm 2\Delta k$ on the same missing spoke.

5.2.3. DCE prostate datasets

DCE imaging was performed on a Siemens 7T Magnetome scanner equipped with a 16-channel flexible body transceiver array coil using a custom UTE sequence. The prostate of a human subject was the target for this DCE study. The temporal resolution is 6s, and the contrast delivered was 0.2 mmol/kg gadobutrol at a rate of 2ml/s. The imaging parameters were: FOV 300×300×96mm^3, spatial resolution 1×1×3mm^3, TE/TR=0.42/3ms, scan time 5 minutes. A 2D Halton sequence was mapped onto the surface of a cylindrical k-space by $k_{xy}(t) = k_x(t) + ik_y(t) = \gamma \int G_{rad}(t) e^{i2\pi\alpha} dt$ and $k_z(t) = k_z^{max}(2\beta - 1)$. The in-plane k-space coordinates and the phase-encoding slices are represented by $k_{xy}(t)$ and $k_z(t)$, respectively. The resultant 3D k-space trajectories are illustrated in Figure 16. Each set of 2048 spokes, acquired during a period 6s of standard temporal resolution, corresponds to an effective acceleration rate of R=15.

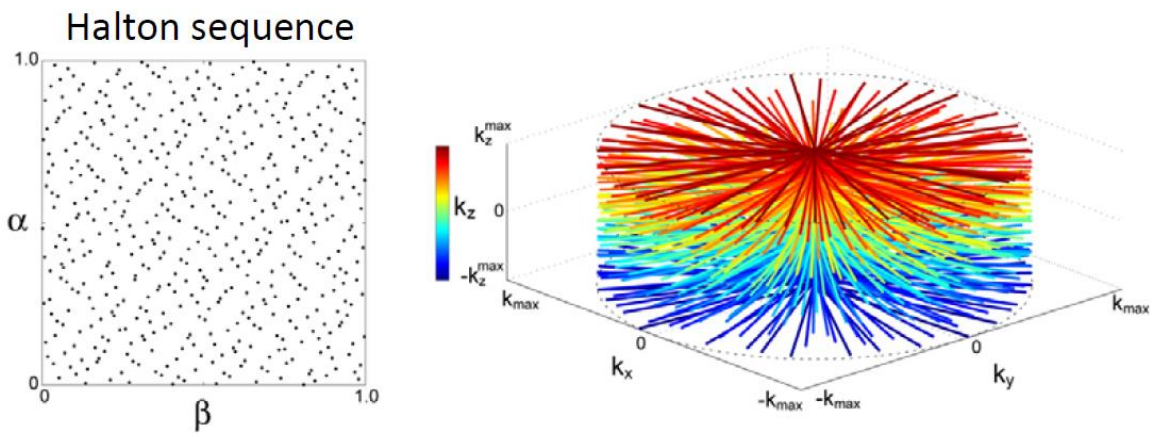

Figure 16: The stack-of-stars sampling with a 2D Halton sequence.

5.2.4. Reconstruction experiments

A fully sampled composite dataset was generated by combining all 51 time frames. It was then gridded to a Cartesian ACS dataset, from which different RIKs were calibrated using the central three k_z planes. SING reconstruction was compared to CS reconstruction which was implemented with the spatial and the temporal total variation constraints[201], unregularized CG-SENSE[22] and gridding reconstruction.

5.3. Results

Figure 17 shows the two selected zoomed regions from the central slice of gridding, CG-SENSE, CS and SING reconstructions at the selected time frame in the wash-out phase. This time frame has 2048 spokes (R=15) which were acquired with standard 6s temporal resolution. The gridding reconstruction of 30720 spokes (R=1) acquired nearest to the selected time frame is used as the reference image.

Gridding image (R=15) shows streaking and blurring artifacts. CG-SENSE image has visually noticeable noise amplification at R=15. CS reconstruction is slightly blurred (red arrows) at R=15, while SING shows improved delineation of the tissues in the prostate with moderate noise amplification. For CS reconstruction the use of total variation (TV) in the spatial domain may reduce spatial noise while sacrificing spatial resolution. The TV regularization parameter was empirically selected, and the optimization of parameter may lead to improved sharpness in the CS reconstruction.

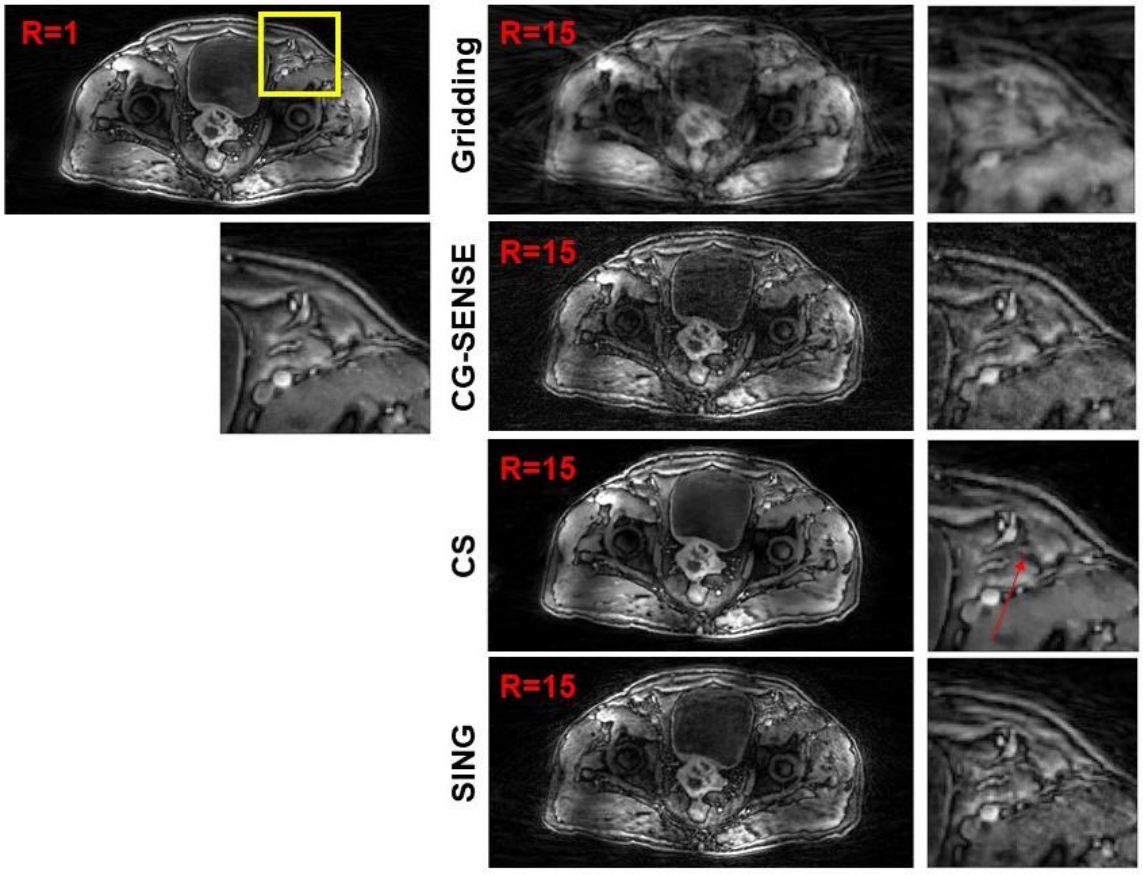

Figure 17: A selected zoomed regions (yellow box) from the central slice of gridding, CG-SENSE (un-regularized), CS and SING reconstructions of 2048

spokes (R=15) acquired during the wash-out phase. The reference image (top-left) is gridding reconstruction of 30720 spokes (R=1).

5.4. Discussion

SING enables the k-space reconstruction of different parts of k-space using different interpolation kernels which has shown superior reconstruction than alternative kernels including angular-independent/readout-dependent kernels. The primary advantage of SING is that it eliminates the need for separate calibration scans, while preserving the reconstruction quality. In addition, SING enables the reconstruction of high-quality dynamic images without exploiting temporal constraints which require empirical determination of parameter (inappropriate selection of parameter can lead to temporal artifacts in reconstructed images of dynamic series). The SNR regularized calibration of RIKs stabilizes the signal contributions for the data reconstruction in the presence of noise. The reconstructions of signals with varying SNR at different k-space regions can be adapted, while also eliminating the need for selecting different regularization parameters.

Chapter 6

Conclusion

6.1. Thesis Summary

The main objective of this research was to address the challenges of calibrating RIKs and the scalability issues which are mainly due to lengthy scanning times. To address these issues, we developed a non-Cartesian k-space reconstruction method, referred to as SING, using self-calibrated RIKs for accelerated 2D and 3D non-Cartesian acquisitions. The results on 2D/3D non-Cartesian dynamic/anatomical imaging were provided in Chapters 3-5.

In Chapter 3, 2D-SING was developed for accelerated 2D radial imaging, while aiming for similar reconstruction quality of TT-GRAPPA without the use of additional ACS data. The proposed local k-space regularization, which explicitly adds noise regularization, enabled successful reconstruction. This noise regularization was applied to emulate the inherent regularization effect of additional acquired ACS data in TT-GRAPPA. In the simulated and the experimental 2D cine datasets, SING has demonstrated reconstruction performance similar to TT-GRAPPA and superior to CG-SENSE.

In Chapter 4, 2D-SING was extended to 3D-SING for the reconstruction of accelerated 3D radial (kooshball) imaging to address the challenge of applying TT-

GRAPPA which is due to lengthy calibration scanning. The 3D extension involved direct scaling of local k-space regularization. Using whole-heart coronary MRI datasets, the results demonstrated the reconstruction efficacy of 3D-SING. When compared with CS, 3D-SING showed fewer visually blurring artifacts. In the comparisons with gridding and CG-SENSE, 3D-SING showed fewer streaking artifacts and noise amplifications.

6.2. Limitations and future work

One limitation of SING is that as the acceleration rate increases, the amount of ACS data decreases. The Nyquist radius, which determines the ACS region, is smaller as the acceleration is increased, leading to smaller set of ACS data and degrading reconstruction quality. One possible solution to this issue is to acquire separate ACS data, and thus the amount of calibration is not reduced as the acceleration rate increases. Furthermore, the number of subjects for testing the method in the thesis is not large enough. In a typical clinical study, the method efficacy should be investigated using sufficient number of testing subjects with distinct profiles, such as age, and physical conditions.

A potential investigation in future work can be performed on the SING efficacy when Cartesian ACS data is acquired rather than interpolated from undersampled data. The acquisition of ACS data avoids the use of Kaiser-Bessel convolution, thereby reducing errors in the interpolation of ACS data and a potential improvement of SING reconstruction. Moreover, while missing data points on non-

Cartesian grid were reconstructed and then gridded to Cartesian grid in current SING reconstruction, missing data points on Cartesian grid can be directly reconstructed and the gridding reconstruction can be avoided. By avoiding the gridding reconstruction, the use of density correction function that generates reconstruction errors can be removed, thereby potentially improving quality of image reconstructions.

References

1. Lauterbur PC. Image formation by induced local interactions. Examples employing nuclear magnetic resonance. 1973. *Clin Orthop Relat Res*. Jul 1989;(244):3-6.
2. Sodickson DK, Manning WJ. Simultaneous acquisition of spatial harmonics (SMASH): fast imaging with radiofrequency coil arrays. *Magn Reson Med*. Oct 1997;38(4):591-603. doi:10.1002/mrm.1910380414
3. Griswold MA, Jakob PM, Heidemann RM, et al. Generalized autocalibrating partially parallel acquisitions (GRAPPA). *Magn Reson Med*. Jun 2002;47(6):1202-10. doi:10.1002/mrm.10171
4. Tsao J, Boesiger P, Pruessmann KP. k-t BLAST and k-t SENSE: dynamic MRI with high frame rate exploiting spatiotemporal correlations. *Magn Reson Med*. Nov 2003;50(5):1031-42. doi:10.1002/mrm.10611
5. Kozerke S, Tsao J, Razavi R, Boesiger P. Accelerating cardiac cine 3D imaging using k-t BLAST. *Magn Reson Med*. Jul 2004;52(1):19-26. doi:10.1002/mrm.20145
6. Madore B, Glover GH, Pelc NJ. Unaliasing by fourier-encoding the overlaps using the temporal dimension (UNFOLD), applied to cardiac imaging and fMRI. *Magn Reson Med*. Nov 1999;42(5):813-28. doi:10.1002/(sici)1522-2594(199911)42:5<813::aid-mrm1>3.0.co;2-s
7. Pruessmann KP, Weiger M, Scheidegger MB, Boesiger P. SENSE: sensitivity encoding for fast MRI. *Magn Reson Med*. Nov 1999;42(5):952-62.
8. Lustig M, Donoho D, Pauly JM. Sparse MRI: The application of compressed sensing for rapid MR imaging. *Magn Reson Med*. Dec 2007;58(6):1182-95. doi:10.1002/mrm.21391
9. Block KT, Uecker M, Frahm J. Undersampled radial MRI with multiple coils. Iterative image reconstruction using a total variation constraint. *Magn Reson Med*. Jun 2007;57(6):1086-98. doi:10.1002/mrm.21236

10. Peters DC, Rohatgi P, Botnar RM, Yeon SB, Kissinger KV, Manning WJ. Characterizing radial undersampling artifacts for cardiac applications. *Magn Reson Med*. Feb 2006;55(2):396-403. doi:10.1002/mrm.20782

11. Glover GH, Pauly JM. Projection reconstruction techniques for reduction of motion effects in MRI. *Magn Reson Med*. Dec 1992;28(2):275-89. doi:10.1002/mrm.1910280209

12. Liao JR, Pauly JM, Brosnan TJ, Pelc NJ. Reduction of motion artifacts in cine MRI using variable-density spiral trajectories. *Magn Reson Med*. Apr 1997;37(4):569-75. doi:10.1002/mrm.1910370416

13. Pipe JG. Motion correction with PROPELLER MRI: application to head motion and free-breathing cardiac imaging. *Magn Reson Med*. Nov 1999;42(5):963-9. doi:10.1002/(sici)1522-2594(199911)42:5<963::aid-mrm17>3.0.co;2-l

14. Liu C, Bammer R, Kim DH, Moseley ME. Self-navigated interleaved spiral (SNAILS): application to high-resolution diffusion tensor imaging. *Magn Reson Med*. Dec 2004;52(6):1388-96. doi:10.1002/mrm.20288

15. Larson AC, White RD, Laub G, McVeigh ER, Li D, Simonetti OP. Self-gated cardiac cine MRI. *Magn Reson Med*. Jan 2004;51(1):93-102. doi:10.1002/mrm.10664

16. Qian Y, Boada FE. Acquisition-weighted stack of spirals for fast high-resolution three-dimensional ultra-short echo time MR imaging. *Magn Reson Med*. Jul 2008;60(1):135-45. doi:10.1002/mrm.21620

17. Noll DC. Multishot rosette trajectories for spectrally selective MR imaging. *IEEE Trans Med Imaging*. Aug 1997;16(4):372-7. doi:10.1109/42.611345

18. Adalsteinsson E, Star-Lack J, Meyer CH, Spielman DM. Reduced spatial side lobes in chemical-shift imaging. *Magn Reson Med*. Aug 1999;42(2):314-23. doi:10.1002/(sici)1522-2594(199908)42:2<314::aid-mrm14>3.0.co;2-x

19. Ahn CB, Kim JH, Cho ZH. High-speed spiral-scan echo planar NMR imaging-I. *IEEE Trans Med Imaging*. 1986;5(1):2-7. doi:10.1109/TMI.1986.4307732

20. Meyer CH, Hu BS, Nishimura DG, Macovski A. Fast spiral coronary artery imaging. *Magn Reson Med*. Dec 1992;28(2):202-13. doi:10.1002/mrm.1910280204
21. Scheffler K, Hennig J. Frequency resolved single-shot MR imaging using stochastic k-space trajectories. *Magn Reson Med*. Apr 1996;35(4):569-76. doi:10.1002/mrm.1910350417
22. Pruessmann KP, Weiger M, Börnert P, Boesiger P. Advances in sensitivity encoding with arbitrary k-space trajectories. *Magn Reson Med*. Oct 2001;46(4):638-51. doi:10.1002/mrm.1241
23. MA G, RM H, PM J. Direct Parallel Imaging Reconstruction of Radially Sampled Data Using GRAPPA with Relative Shifts. 2003:
24. Seiberlich N, Ehses P, Duerk J, Gilkeson R, Griswold M. Improved radial GRAPPA calibration for real-time free-breathing cardiac imaging. *Magn Reson Med*. Feb 2011;65(2):492-505. doi:10.1002/mrm.22618
25. Heidemann RM, Griswold MA, Seiberlich N, et al. Direct parallel image reconstructions for spiral trajectories using GRAPPA. *Magn Reson Med*. Aug 2006;56(2):317-26. doi:10.1002/mrm.20951
26. Seiberlich N, Lee G, Ehses P, Duerk JL, Gilkeson R, Griswold M. Improved temporal resolution in cardiac imaging using through-time spiral GRAPPA. *Magn Reson Med*. Dec 2011;66(6):1682-8. doi:10.1002/mrm.22952
27. Seiberlich N, Breuer F, Heidemann R, Blaimer M, Griswold M, Jakob P. Reconstruction of undersampled non-Cartesian data sets using pseudo-Cartesian GRAPPA in conjunction with GROG. *Magn Reson Med*. May 2008;59(5):1127-37. doi:10.1002/mrm.21602
28. Heberlein K, Hu X. Auto-calibrated parallel spiral imaging. *Magn Reson Med*. Mar 2006;55(3):619-25. doi:10.1002/mrm.20811
29. Lustig M, Pauly JM. SPIRiT: Iterative self-consistent parallel imaging reconstruction from arbitrary k-space. *Magn Reson Med*. Aug 2010;64(2):457-71. doi:10.1002/mrm.22428
30. Griswold MA, Jakob PM, Nittka M, Goldfarb JW, Haase A. Partially parallel imaging with localized sensitivities (PILS). *Magn Reson Med*. Oct

2000;44(4):602-9. doi:10.1002/1522-2594(200010)44:4<602::aid-mrm14>3.0.co;2-5

31. Liu C, Bammer R, Moseley ME. Parallel imaging reconstruction for arbitrary trajectories using k-space sparse matrices (kSPA). *Magn Reson Med*. Dec 2007;58(6):1171-81. doi:10.1002/mrm.21334

32. Samsonov AA, Block WF, Arunachalam A, Field AS. Advances in locally constrained k-space-based parallel MRI. *Magn Reson Med*. Feb 2006;55(2):431-8. doi:10.1002/mrm.20757

33. Hu P, Meyer C. Parallel image reconstruction based on successive convolution operations; Proceedings of the 14th Annual Meeting of ISMRM; Seattle. 2006:p.10.

34. Feng L, Axel L, Chandarana H, Block KT, Sodickson DK, Otazo R. XD-GRASP: Golden-angle radial MRI with reconstruction of extra motion-state dimensions using compressed sensing. *Magn Reson Med*. Feb 2016;75(2):775-88. doi:10.1002/mrm.25665

35. Nam S, Akçakaya M, Basha T, et al. Compressed sensing reconstruction for whole-heart imaging with 3D radial trajectories: a graphics processing unit implementation. *Magn Reson Med*. Jan 2013;69(1):91-102. doi:10.1002/mrm.24234

36. Breuer FA, Kannengiesser SA, Blaimer M, Seiberlich N, Jakob PM, Griswold MA. General formulation for quantitative G-factor calculation in GRAPPA reconstructions. *Magn Reson Med*. Sep 2009;62(3):739-46. doi:10.1002/mrm.22066

37. Saybasili H, Herzka DA, Seiberlich N, Griswold MA. Real-time imaging with radial GRAPPA: Implementation on a heterogeneous architecture for low-latency reconstructions. *Magn Reson Imaging*. Jul 2014;32(6):747-58. doi:10.1016/j.mri.2014.02.022

38. Carr JC, Simonetti O, Bundy J, Li D, Pereles S, Finn JP. Cine MR angiography of the heart with segmented true fast imaging with steady-state precession. *Radiology*. Jun 2001;219(3):828-34. doi:10.1148/radiology.219.3.r01jn44828

39. Kramer CM, Barkhausen J, Flamm SD, Kim RJ, Nagel E, Protocols SfCMRBoTTFoS. Standardized cardiovascular magnetic resonance (CMR) protocols 2013 update. *J Cardiovasc Magn Reson*. Oct 2013;15:91. doi:10.1186/1532-429X-15-91

40. Atkinson DJ, Edelman RR. Cineangiography of the heart in a single breath hold with a segmented turboFLASH sequence. *Radiology*. Feb 1991;178(2):357-60. doi:10.1148/radiology.178.2.1987592

41. Edelman RR, Chien D, Kim D. Fast selective black blood MR imaging. *Radiology*. Dec 1991;181(3):655-60. doi:10.1148/radiology.181.3.1947077

42. Judd RM, Reeder SB, Atalar E, McVeigh ER, Zerhouni EA. A magnetization-driven gradient echo pulse sequence for the study of myocardial perfusion. *Magn Reson Med*. Aug 1995;34(2):276-82. doi:10.1002/mrm.1910340220

43. Payne AR, Casey M, McClure J, et al. Bright-blood T2-weighted MRI has higher diagnostic accuracy than dark-blood short tau inversion recovery MRI for detection of acute myocardial infarction and for assessment of the ischemic area at risk and myocardial salvage. *Circ Cardiovasc Imaging*. May 2011;4(3):210-9. doi:10.1161/CIRCIMAGING.110.960450

44. Ridgway JP. Cardiovascular magnetic resonance physics for clinicians: part I. *J Cardiovasc Magn Reson*. Nov 2010;12:71. doi:10.1186/1532-429X-12-71

45. van der Geest RJ, Reiber JH. Quantification in cardiac MRI. *J Magn Reson Imaging*. Nov 1999;10(5):602-8. doi:10.1002/(sici)1522-2586(199911)10:5<602::aid-jmri3>3.0.co;2-c

46. Ferreira VM, Piechnik SK, Dall'Armellina E, et al. Native T1-mapping detects the location, extent and patterns of acute myocarditis without the need for gadolinium contrast agents. *J Cardiovasc Magn Reson*. May 2014;16:36. doi:10.1186/1532-429X-16-36

47. Haase A, Matthaei D, Bartkowski R, Dühmke E, Leibfritz D. Inversion recovery snapshot FLASH MR imaging. *J Comput Assist Tomogr*. 1989 Nov-Dec 1989;13(6):1036-40. doi:10.1097/00004728-198911000-00016

48. Ding S, Wolff SD, Epstein FH. Improved coverage in dynamic contrast-enhanced cardiac MRI using interleaved gradient-echo EPI. *Magn Reson Med*. Apr 1998;39(4):514-9. doi:10.1002/mrm.1910390403
49. Schreiber WG, Schmitt M, Kalden P, Mohrs OK, Kreitner KF, Thelen M. Dynamic contrast-enhanced myocardial perfusion imaging using saturation-prepared TrueFISP. *J Magn Reson Imaging*. Dec 2002;16(6):641-52. doi:10.1002/jmri.10209
50. Plein S, Radjenovic A, Ridgway JP, et al. Coronary artery disease: myocardial perfusion MR imaging with sensitivity encoding versus conventional angiography. *Radiology*. May 2005;235(2):423-30. doi:10.1148/radiol.2352040454
51. Pruessmann KP, Weiger M, Boesiger P. Sensitivity encoded cardiac MRI. *J Cardiovasc Magn Reson*. 2001;3(1):1-9. doi:10.1081/jcmr-100000143
52. Mistretta CA, Wieben O, Velikina J, et al. Highly constrained backprojection for time-resolved MRI. *Magn Reson Med*. Jan 2006;55(1):30-40. doi:10.1002/mrm.20772
53. Ma H, Yang J, Liu J, et al. Myocardial perfusion magnetic resonance imaging using sliding-window conjugate-gradient highly constrained back-projection reconstruction for detection of coronary artery disease. *Am J Cardiol*. Apr 2012;109(8):1137-41. doi:10.1016/j.amjcard.2011.11.051
54. Plein S, Ryf S, Schwitter J, Radjenovic A, Boesiger P, Kozerke S. Dynamic contrast-enhanced myocardial perfusion MRI accelerated with k-t sense. *Magn Reson Med*. Oct 2007;58(4):777-85. doi:10.1002/mrm.21381
55. Otazo R, Kim D, Axel L, Sodickson DK. Combination of compressed sensing and parallel imaging for highly accelerated first-pass cardiac perfusion MRI. *Magn Reson Med*. Sep 2010;64(3):767-76. doi:10.1002/mrm.22463
56. Kramer CM, Barkhausen J, Flamm SD, Kim RJ, Nagel E, Protocols SfCMRBoTTFoS. Standardized cardiovascular magnetic resonance imaging (CMR) protocols, society for cardiovascular magnetic resonance: board of trustees task force on standardized protocols. *J Cardiovasc Magn Reson*. Jul 2008;10:35. doi:10.1186/1532-429X-10-35

57. Schalla S, Klein C, Paetsch I, et al. Real-time MR image acquisition during high-dose dobutamine hydrochloride stress for detecting left ventricular wall-motion abnormalities in patients with coronary arterial disease. *Radiology*. Sep 2002;224(3):845-51. doi:10.1148/radiol.2243010945

58. Ratner AV, Okada RD, Newell JB, Pohost GM. The relationship between proton nuclear magnetic resonance relaxation parameters and myocardial perfusion with acute coronary arterial occlusion and reperfusion. *Circulation*. Apr 1985;71(4):823-8. doi:10.1161/01.cir.71.4.823

59. Johnston DL, Brady TJ, Ratner AV, et al. Assessment of myocardial ischemia with proton magnetic resonance: effects of a three hour coronary occlusion with and without reperfusion. *Circulation*. Mar 1985;71(3):595-601. doi:10.1161/01.cir.71.3.595

60. Pflugfelder PW, Wisenberg G, Prato FS, Carroll SE, Turner KL. Early detection of canine myocardial infarction by magnetic resonance imaging in vivo. *Circulation*. Mar 1985;71(3):587-94. doi:10.1161/01.cir.71.3.587

61. Pereira RS, Prato FS, Sykes J, Wisenberg G. Assessment of myocardial viability using MRI during a constant infusion of Gd-DTPA: further studies at early and late periods of reperfusion. *Magn Reson Med*. Jul 1999;42(1):60-8. doi:10.1002/(sici)1522-2594(199907)42:1<60::aid-mrm10>3.0.co;2-9

62. Rogers WJ, Kramer CM, Geskin G, et al. Early contrast-enhanced MRI predicts late functional recovery after reperfused myocardial infarction. *Circulation*. Feb 1999;99(6):744-50. doi:10.1161/01.cir.99.6.744

63. Morse OC, Singer JR. Blood velocity measurements in intact subjects. *Science*. Oct 1970;170(3956):440-1. doi:10.1126/science.170.3956.440

64. Rittgers SE, Fei DY, Kraft KA, Fatouros PP, Kishore PR. Velocity profiles in stenosed tube models using magnetic resonance imaging. *J Biomech Eng*. Aug 1988;110(3):180-4. doi:10.1115/1.3108428

65. Oshinski JN, Ku DN, Pettigrew RI. Turbulent fluctuation velocity: the most significant determinant of signal loss in stenotic vessels. *Magn Reson Med*. Feb 1995;33(2):193-9. doi:10.1002/mrm.1910330208

66. Guilfoyle DN, Gibbs P, Ordidge RJ, Mansfield P. Real-time flow measurements using echo-planar imaging. *Magn Reson Med*. Mar 1991;18(1):1-8. doi:10.1002/mrm.1910180102

67. Keegan J, Gatehouse PD, Yang GZ, Firmin DN. Spiral phase velocity mapping of left and right coronary artery blood flow: correction for through-plane motion using selective fat-only excitation. *J Magn Reson Imaging*. Dec 2004;20(6):953-60. doi:10.1002/jmri.20208

68. Markl M, Alley MT, Pelc NJ. Balanced phase-contrast steady-state free precession (PC-SSFP): a novel technique for velocity encoding by gradient inversion. *Magn Reson Med*. May 2003;49(5):945-52. doi:10.1002/mrm.10451

69. Haase A. Snapshot FLASH MRI. Applications to T1, T2, and chemical-shift imaging. *Magn Reson Med*. Jan 1990;13(1):77-89. doi:10.1002/mrm.1910130109

70. Gyngell ML. The application of steady-state free precession in rapid 2DFT NMR imaging: FAST and CE-FAST sequences. *Magn Reson Imaging*. 1988 Jul-Aug 1988;6(4):415-9. doi:10.1016/0730-725x(88)90478-x

71. Wang HZ, Riederer SJ. A spoiling sequence for suppression of residual transverse magnetization. *Magn Reson Med*. Aug 1990;15(2):175-91. doi:10.1002/mrm.1910150202

72. Graumann R, Fischer H, Oppelt A. A new pulse sequence for determining T1 and T2 simultaneously. *Med Phys*. 1986 Sep-Oct 1986;13(5):644-7. doi:10.1118/1.595867

73. Larsson HB, Stubgaard M, Frederiksen JL, Jensen M, Henriksen O, Paulson OB. Quantitation of blood-brain barrier defect by magnetic resonance imaging and gadolinium-DTPA in patients with multiple sclerosis and brain tumors. *Magn Reson Med*. Oct 1990;16(1):117-31. doi:10.1002/mrm.1910160111

74. Brix G, Semmler W, Port R, Schad LR, Layer G, Lorenz WJ. Pharmacokinetic parameters in CNS Gd-DTPA enhanced MR imaging. *J Comput Assist Tomogr*. 1991 Jul-Aug 1991;15(4):621-8. doi:10.1097/00004728-199107000-00018

75. Tofts PS. Optimal detection of blood-brain barrier defects with Gd-DTPA MRI-the influences of delayed imaging and optimised repetition time. *Magn Reson Imaging*. 1996;14(4):373-80. doi:10.1016/0730-725x(96)00023-9
76. Tofts PS. Modeling tracer kinetics in dynamic Gd-DTPA MR imaging. *J Magn Reson Imaging*. 1997 Jan-Feb 1997;7(1):91-101. doi:10.1002/jmri.1880070113
77. Tofts PS, Berkowitz B, Schnall MD. Quantitative analysis of dynamic Gd-DTPA enhancement in breast tumors using a permeability model. *Magn Reson Med*. Apr 1995;33(4):564-8. doi:10.1002/mrm.1910330416
78. St Lawrence KS, Lee TY. An adiabatic approximation to the tissue homogeneity model for water exchange in the brain: I. Theoretical derivation. *J Cereb Blood Flow Metab*. Dec 1998;18(12):1365-77. doi:10.1097/00004647-199812000-00011
79. Tofts PS, Kermode AG. Measurement of the blood-brain barrier permeability and leakage space using dynamic MR imaging. 1. Fundamental concepts. *Magn Reson Med*. Feb 1991;17(2):357-67. doi:10.1002/mrm.1910170208
80. Wintersperger BJ, Reeder SB, Nikolaou K, et al. Cardiac CINE MR imaging with a 32-channel cardiac coil and parallel imaging: impact of acceleration factors on image quality and volumetric accuracy. *J Magn Reson Imaging*. Feb 2006;23(2):222-7. doi:10.1002/jmri.20484
81. Fenchel M, Deshpande VS, Nael K, et al. Cardiac cine imaging at 3 Tesla: initial experience with a 32-element body-array coil. *Invest Radiol*. Aug 2006;41(8):601-8. doi:10.1097/01.rli.0000223896.70095.49
82. Hardy CJ, Cline HE, Giaquinto RO, Niendorf T, Grant AK, Sodickson DK. 32-element receiver-coil array for cardiac imaging. *Magn Reson Med*. May 2006;55(5):1142-9. doi:10.1002/mrm.20870
83. Kellman P, Epstein FH, McVeigh ER. Adaptive sensitivity encoding incorporating temporal filtering (TSENSE). *Magn Reson Med*. May 2001;45(5):846-52. doi:10.1002/mrm.1113

84. Breuer FA, Kellman P, Griswold MA, Jakob PM. Dynamic autocalibrated parallel imaging using temporal GRAPPA (TGRAPPA). *Magn Reson Med*. Apr 2005;53(4):981-5. doi:10.1002/mrm.20430

85. Guttman MA, Kellman P, Dick AJ, Lederman RJ, McVeigh ER. Real-time accelerated interactive MRI with adaptive TSENSE and UNFOLD. *Magn Reson Med*. Aug 2003;50(2):315-21. doi:10.1002/mrm.10504

86. Huang F, Akao J, Vijayakumar S, Duensing GR, Limkeman M. k-t GRAPPA: a k-space implementation for dynamic MRI with high reduction factor. *Magn Reson Med*. Nov 2005;54(5):1172-84. doi:10.1002/mrm.20641

87. van Vaals JJ, Brummer ME, Dixon WT, et al. "Keyhole" method for accelerating imaging of contrast agent uptake. *J Magn Reson Imaging*. 1993 Jul-Aug 1993;3(4):671-5. doi:10.1002/jmri.1880030419

88. Jung H, Sung K, Nayak KS, Kim EY, Ye JC. k-t FOCUSS: a general compressed sensing framework for high resolution dynamic MRI. *Magn Reson Med*. Jan 2009;61(1):103-16. doi:10.1002/mrm.21757

89. Smith DS, Welch EB, Li X, et al. Quantitative effects of using compressed sensing in dynamic contrast enhanced MRI. *Phys Med Biol*. Aug 2011;56(15):4933-46. doi:10.1088/0031-9155/56/15/018

90. Gamper U, Boesiger P, Kozerke S. Compressed sensing in dynamic MRI. *Magn Reson Med*. Feb 2008;59(2):365-73. doi:10.1002/mrm.21477

91. Akçakaya M, Basha TA, Pflugi S, et al. Localized spatio-temporal constraints for accelerated CMR perfusion. *Magn Reson Med*. Sep 2014;72(3):629-39. doi:10.1002/mrm.24963

92. Vincenti G, Monney P, Chaptinel J, et al. Compressed sensing single-breath-hold CMR for fast quantification of LV function, volumes, and mass. *JACC Cardiovasc Imaging*. Sep 2014;7(9):882-92. doi:10.1016/j.jcmg.2014.04.016

93. Barkauskas KJ, Rajiah P, Ashwath R, et al. Quantification of left ventricular functional parameter values using 3D spiral bSSFP and through-time non-Cartesian GRAPPA. *J Cardiovasc Magn Reson*. Sep 2014;16:65. doi:10.1186/s12968-014-0065-1

94. Smith DS, Li X, Abramson RG, Quarles CC, Yankeelov TE, Welch EB. Potential of compressed sensing in quantitative MR imaging of cancer. *Cancer Imaging*. Dec 2013;13(4):633-44. doi:10.1102/1470-7330.2013.0041
95. Lustig M, S. JM, D. D, M. PJ. k-t SPARSE: high frame rate dynamic MRI exploiting spatio-temporal sparsity," in Proceedings of the 13th Annual Meeting of ISMRM, vol. 2420, Seattle, Wash, USA, 2006. 2006:
96. Lingala SG, Hu Y, DiBella E, Jacob M. Accelerated dynamic MRI exploiting sparsity and low-rank structure: k-t SLR. *IEEE Trans Med Imaging*. May 2011;30(5):1042-54. doi:10.1109/TMI.2010.2100850
97. Feng L, Grimm R, Block KT, et al. Golden-angle radial sparse parallel MRI: combination of compressed sensing, parallel imaging, and golden-angle radial sampling for fast and flexible dynamic volumetric MRI. *Magn Reson Med*. Sep 2014;72(3):707-17. doi:10.1002/mrm.24980
98. J. J, T. L. Dynamic MRI with compressed sensing imaging using temporal correlations, in Proceedings of the 5th IEEE

International Symposium on Biomedical Imaging: From Nano to Macro (ISBI '08), pp. 1613–1616, Paris, France, May 2008. 2008:
99. Niendorf T, Sodickson DK. Parallel imaging in cardiovascular MRI: methods and applications. *NMR Biomed*. May 2006;19(3):325-41. doi:10.1002/nbm.1051
100. Hendel RC ea. ACCF/ACR/SCCT/SCMR/ASNC/NASCI/ SCAI/SIR 2006 appropriateness criteria for cardiac computed tomography and cardiac magnetic resonance imaging: a report of the American College of Cardiology Foundation Quality Strategic Directions Committee Appropriateness Criteria Working Group, American College of Radiology, Society of Cardiovascular Computed Tomography, Society for Cardiovascular Magnetic Resonance, American Society of Nuclear Cardiology, North American Society for Cardiac Imaging, Society for Cardiovascular Angiography and Interventions, and Society of Interventional Radiology *J Am Coll Cardiol*. 2006;48(7):1475–97.
101. Hundley WG ea. ACCF/ACR/AHA/NASCI/SCMR 2010 expert consensus document on cardiovascular magnetic resonance. A report of the American

College of Cardiology Foundation Task Force on Expert Consensus Documents. . *Circulation*. 2010;121:2462–508.

102. Manning WJ, Edelman RR. Magnetic resonance coronary angiography. *Magn Reson Q*. Sep 1993;9(3):131-51.

103. Kim WY, Danias PG, Stuber M, et al. Coronary magnetic resonance angiography for the detection of coronary stenoses. *N Engl J Med*. Dec 2001;345(26):1863-9. doi:10.1056/NEJMoa010866

104. Stuber M, Botnar RM, Danias PG, Kissinger KV, Manning WJ. Breathhold three-dimensional coronary magnetic resonance angiography using real-time navigator technology. *J Cardiovasc Magn Reson*. 1999;1(3):233-8. doi:10.3109/10976649909088335

105. Stuber M, Botnar RM, Danias PG, Kissinger KV, Manning WJ. Submillimeter three-dimensional coronary MR angiography with real-time navigator correction: comparison of navigator locations. *Radiology*. Aug 1999;212(2):579-87. doi:10.1148/radiology.212.2.r99au50579

106. Stuber M, Botnar RM, Danias PG, et al. Double-oblique free-breathing high resolution three-dimensional coronary magnetic resonance angiography. *J Am Coll Cardiol*. Aug 1999;34(2):524-31. doi:10.1016/s0735-1097(99)00223-5

107. Bhat H, Zuehlsdorff S, Bi X, Li D. Whole-heart contrast-enhanced coronary magnetic resonance angiography using gradient echo interleaved EPI. *Magn Reson Med*. Jun 2009;61(6):1388-95. doi:10.1002/mrm.21963

108. Bi X, Carr JC, Li D. Whole-heart coronary magnetic resonance angiography at 3 Tesla in 5 minutes with slow infusion of Gd-BOPTA, a high-relaxivity clinical contrast agent. *Magn Reson Med*. Jul 2007;58(1):1-7. doi:10.1002/mrm.21224

109. Bi X, Deshpande V, Carr J, Li D. Coronary artery magnetic resonance angiography (MRA): a comparison between the whole-heart and volume-targeted methods using a T2-prepared SSFP sequence. *J Cardiovasc Magn Reson*. 2006;8(5):703-7. doi:10.1080/10976640600723706

110. Kim YJ, Seo JS, Choi BW, Choe KO, Jang Y, Ko YG. Feasibility and diagnostic accuracy of whole heart coronary MR angiography using free-

breathing 3D balanced turbo-field-echo with SENSE and the half-fourier acquisition technique. *Korean J Radiol*. 2006 Oct-Dec 2006;7(4):235-42. doi:10.3348/kjr.2006.7.4.235

111. Lai P, Bi X, Jerecic R, Li D. A respiratory self-gating technique with 3D-translation compensation for free-breathing whole-heart coronary MRA. *Magn Reson Med*. Sep 2009;62(3):731-8. doi:10.1002/mrm.22058

112. Lai P, Larson AC, Bi X, Jerecic R, Li D. A dual-projection respiratory self-gating technique for whole-heart coronary MRA. *J Magn Reson Imaging*. Sep 2008;28(3):612-20. doi:10.1002/jmri.21479

113. Liu X, Bi X, Huang J, Jerecic R, Carr J, Li D. Contrast-enhanced whole-heart coronary magnetic resonance angiography at 3.0 T: comparison with steady-state free precession technique at 1.5 T. *Invest Radiol*. Sep 2008;43(9):663-8. doi:10.1097/RLI.0b013e31817ed1ff

114. Maintz D, Ozgun M, Hoffmeier A, et al. Whole-heart coronary magnetic resonance angiography: value for the detection of coronary artery stenoses in comparison to multislice computed tomography angiography. *Acta Radiol*. Nov 2007;48(9):967-73. doi:10.1080/02841850701630292

115. Nehrke K, Börnert P, Mazurkewitz P, Winkelmann R, Grässlin I. Free-breathing whole-heart coronary MR angiography on a clinical scanner in four minutes. *J Magn Reson Imaging*. May 2006;23(5):752-6. doi:10.1002/jmri.20559

116. Niendorf T, Hardy CJ, Giaquinto RO, et al. Toward single breath-hold whole-heart coverage coronary MRA using highly accelerated parallel imaging with a 32-channel MR system. *Magn Reson Med*. Jul 2006;56(1):167-76. doi:10.1002/mrm.20923

117. Okada T, Kanao S, Ninomiya A, et al. Whole-heart coronary magnetic resonance angiography with parallel imaging: comparison of acceleration in one-dimension vs. two-dimensions. *Eur J Radiol*. Sep 2009;71(3):486-91. doi:10.1016/j.ejrad.2008.06.005

118. Sakuma H, Ichikawa Y, Chino S, Hirano T, Makino K, Takeda K. Detection of coronary artery stenosis with whole-heart coronary magnetic resonance

angiography. *J Am Coll Cardiol*. Nov 2006;48(10):1946-50. doi:10.1016/j.jacc.2006.07.055

119. Sakuma H, Ichikawa Y, Suzawa N, et al. Assessment of coronary arteries with total study time of less than 30 minutes by using whole-heart coronary MR angiography. *Radiology*. Oct 2005;237(1):316-21. doi:10.1148/radiol.2371040830

120. Stehning C, Börnert P, Nehrke K, Eggers H, Stuber M. Free-breathing whole-heart coronary MRA with 3D radial SSFP and self-navigated image reconstruction. *Magn Reson Med*. Aug 2005;54(2):476-80. doi:10.1002/mrm.20557

121. Weber OM, Martin AJ, Higgins CB. Whole-heart steady-state free precession coronary artery magnetic resonance angiography. *Magn Reson Med*. Dec 2003;50(6):1223-8. doi:10.1002/mrm.10653

122. Maintz D, Aepfelbacher FC, Kissinger KV, et al. Coronary MR angiography: comparison of quantitative and qualitative data from four techniques. *AJR Am J Roentgenol*. Feb 2004;182(2):515-21. doi:10.2214/ajr.182.2.1820515

123. Ozgun M, Hoffmeier A, Kouwenhoven M, et al. Comparison of 3D segmented gradient-echo and steady-state free precession coronary MRI sequences in patients with coronary artery disease. *AJR Am J Roentgenol*. Jul 2005;185(1):103-9. doi:10.2214/ajr.185.1.01850103

124. Nezafat R, Herzka D, Stehning C, Peters DC, Nehrke K, Manning WJ. Inflow quantification in three-dimensional cardiovascular MR imaging. *J Magn Reson Imaging*. Nov 2008;28(5):1273-9. doi:10.1002/jmri.21493

125. Weber OM, Pujadas S, Martin AJ, Higgins CB. Free-breathing, three-dimensional coronary artery magnetic resonance angiography: comparison of sequences. *J Magn Reson Imaging*. Sep 2004;20(3):395-402. doi:10.1002/jmri.20141

126. Katoh M, Spuentrup E, Buecker A, Manning WJ, Günther RW, Botnar RM. MR coronary vessel wall imaging: comparison between radial and spiral k-space

sampling. *J Magn Reson Imaging*. May 2006;23(5):757-62. doi:10.1002/jmri.20569

127. Park J, Larson AC, Zhang Q, Simonetti O, Li D. 4D radial coronary artery imaging within a single breath-hold: cine angiography with phase-sensitive fat suppression (CAPS). *Magn Reson Med*. Oct 2005;54(4):833-40. doi:10.1002/mrm.20627

128. Yang Q, Li K, Liu X, et al. Contrast-enhanced whole-heart coronary magnetic resonance angiography at 3.0-T: a comparative study with X-ray angiography in a single center. *J Am Coll Cardiol*. Jun 2009;54(1):69-76. doi:10.1016/j.jacc.2009.03.016

129. Tang L, Merkle N, Schär M, et al. Volume-targeted and whole-heart coronary magnetic resonance angiography using an intravascular contrast agent. *J Magn Reson Imaging*. Nov 2009;30(5):1191-6. doi:10.1002/jmri.21903

130. Hu P, Chan J, Ngo LH, et al. Contrast-enhanced whole-heart coronary MRI with bolus infusion of gadobenate dimeglumine at 1.5 T. *Magn Reson Med*. Feb 2011;65(2):392-8. doi:10.1002/mrm.22706

131. Nagata M, Kato S, Kitagawa K, et al. Diagnostic accuracy of 1.5-T unenhanced whole-heart coronary MR angiography performed with 32-channel cardiac coils: initial single-center experience. *Radiology*. May 2011;259(2):384-92. doi:10.1148/radiol.11101323

132. Akçakaya M, Basha TA, Goddu B, et al. Low-dimensional-structure self-learning and thresholding: regularization beyond compressed sensing for MRI reconstruction. *Magn Reson Med*. Sep 2011;66(3):756-67. doi:10.1002/mrm.22841

133. Akçakaya M, Basha TA, Chan RH, et al. Accelerated contrast-enhanced whole-heart coronary MRI using low-dimensional-structure self-learning and thresholding. *Magn Reson Med*. May 2012;67(5):1434-43. doi:10.1002/mrm.24242

134. Akçakaya M, Basha TA, Chan RH, Manning WJ, Nezafat R. Accelerated isotropic sub-millimeter whole-heart coronary MRI: compressed sensing versus

parallel imaging. *Magn Reson Med*. Feb 2014;71(2):815-22. doi:10.1002/mrm.24683

135. Santos JM, Cunningham CH, Lustig M, et al. Single breath-hold whole-heart MRA using variable-density spirals at 3T. *Magn Reson Med*. Feb 2006;55(2):371-9. doi:10.1002/mrm.20765

136. Muthurangu V, Lurz P, Critchely JD, Deanfield JE, Taylor AM, Hansen MS. Real-time assessment of right and left ventricular volumes and function in patients with congenital heart disease by using high spatiotemporal resolution radial k-t SENSE. *Radiology*. Sep 2008;248(3):782-91. doi:10.1148/radiol.2482071717

137. Boubertakh R, Prieto C, Batchelor PG, et al. Whole-heart imaging using undersampled radial phase encoding (RPE) and iterative sensitivity encoding (SENSE) reconstruction. *Magn Reson Med*. Nov 2009;62(5):1331-7. doi:10.1002/mrm.22102

138. Kolbitsch C, Prieto C, Smink J, Schaeffter T. Highly efficient whole-heart imaging using radial phase encoding-phase ordering with automatic window selection. *Magn Reson Med*. Oct 2011;66(4):1008-18. doi:10.1002/mrm.22888

139. Krämer M, Herrmann KH, Biermann J, Reichenbach JR. Retrospective reconstruction of cardiac cine images from golden-ratio radial MRI using one-dimensional navigators. *J Magn Reson Imaging*. Aug 2014;40(2):413-22. doi:10.1002/jmri.24364

140. Prieto C, Uribe S, Razavi R, Atkinson D, Schaeffter T. 3D undersampled golden-radial phase encoding for DCE-MRA using inherently regularized iterative SENSE. *Magn Reson Med*. Aug 2010;64(2):514-26. doi:10.1002/mrm.22446

141. Jeong HJ, Cashen TA, Hurley MC, et al. Radial sliding-window magnetic resonance angiography (MRA) with highly-constrained projection reconstruction (HYPR). *Magn Reson Med*. May 2009;61(5):1103-13. doi:10.1002/mrm.21888

142. Wright KL, Lee GR, Ehses P, Griswold MA, Gulani V, Seiberlich N. Three-dimensional through-time radial GRAPPA for renal MR angiography. *J Magn Reson Imaging*. Oct 2014;40(4):864-74. doi:10.1002/jmri.24439

143. Wang K, Busse RF, Holmes JH, et al. Interleaved variable density sampling with a constrained parallel imaging reconstruction for dynamic contrast-enhanced MR angiography. *Magn Reson Med*. Aug 2011;66(2):428-36. doi:10.1002/mrm.22814
144. Wright KL, Chen Y, Saybasili H, Griswold MA, Seiberlich N, Gulani V. Quantitative high-resolution renal perfusion imaging using 3-dimensional through-time radial generalized autocalibrating partially parallel acquisition. *Invest Radiol*. Oct 2014;49(10):666-74. doi:10.1097/RLI.0000000000000070
145. Aandal G, Nadig V, Yeh V, et al. Evaluation of left ventricular ejection fraction using through-time radial GRAPPA. *J Cardiovasc Magn Reson*. Oct 2014;16:79. doi:10.1186/s12968-014-0079-8
146. Lingala SG, Zhu Y, Lim Y, et al. Feasibility of through-time spiral generalized autocalibrating partial parallel acquisition for low latency accelerated real-time MRI of speech. *Magn Reson Med*. Dec 2017;78(6):2275-2282. doi:10.1002/mrm.26611
147. Chen Y, Lo WC, Hamilton JI, et al. Single breath-hold 3D cardiac T1 mapping using through-time spiral GRAPPA. *NMR Biomed*. 06 2018;31(6):e3923. doi:10.1002/nbm.3923
148. Chieh S, Kaveh M, Akcakaya M, Moeller S. A scalable composite through-time radial GRAAPPA method; Proceedings of the 25th Annual Meeting of ISMRM, 2016, Honolulu, HI, USA. 2016:4060.
149. Luo T, Noll DC, Fessler JA, Nielsen JF. A GRAPPA algorithm for arbitrary 2D/3D non-Cartesian sampling trajectories with rapid calibration. *Magn Reson Med*. 09 2019;82(3):1101-1112. doi:10.1002/mrm.27801
150. Beatty PJ, Nishimura DG, Pauly JM. Rapid gridding reconstruction with a minimal oversampling ratio. *IEEE Trans Med Imaging*. Jun 2005;24(6):799-808. doi:10.1109/TMI.2005.848376
151. Qu P, Wang C, Shen GX. Discrepancy-based adaptive regularization for GRAPPA reconstruction. *J Magn Reson Imaging*. Jul 2006;24(1):248-55. doi:10.1002/jmri.20620

152. Chang Y, Liang D, Ying L. Nonlinear GRAPPA: a kernel approach to parallel MRI reconstruction. *Magn Reson Med*. Sep 2012;68(3):730-40. doi:10.1002/mrm.23279
153. Sodickson DK. Tailored SMASH image reconstructions for robust in vivo parallel MR imaging. *Magn Reson Med*. Aug 2000;44(2):243-51. doi:10.1002/1522-2594(200008)44:2<243::aid-mrm11>3.0.co;2-l
154. Yeh EN, McKenzie CA, Ohliger MA, Sodickson DK. Parallel magnetic resonance imaging with adaptive radius in k-space (PARS): constrained image reconstruction using k-space locality in radiofrequency coil encoded data. *Magn Reson Med*. Jun 2005;53(6):1383-92. doi:10.1002/mrm.20490
155. Ding Y, Xue H, Ahmad R, Chang TC, Ting ST, Simonetti OP. Paradoxical effect of the signal-to-noise ratio of GRAPPA calibration lines: A quantitative study. *Magn Reson Med*. Jul 2015;74(1):231-239. doi:10.1002/mrm.25385
156. Wissmann L, Santelli C, Segars WP, Kozerke S. MRXCAT: Realistic numerical phantoms for cardiovascular magnetic resonance. *J Cardiovasc Magn Reson*. Aug 2014;16:63. doi:10.1186/s12968-014-0063-3
157. Huang F, Li Y, Vijayakumar S, Hertel S, Duensing GR. High-pass GRAPPA: an image support reduction technique for improved partially parallel imaging. *Magn Reson Med*. Mar 2008;59(3):642-9. doi:10.1002/mrm.21495
158. Uecker M, Lai P, Murphy MJ, et al. ESPIRiT--an eigenvalue approach to autocalibrating parallel MRI: where SENSE meets GRAPPA. *Magn Reson Med*. Mar 2014;71(3):990-1001. doi:10.1002/mrm.24751
159. Robson PM, Grant AK, Madhuranthakam AJ, Lattanzi R, Sodickson DK, McKenzie CA. Comprehensive quantification of signal-to-noise ratio and g-factor for image-based and k-space-based parallel imaging reconstructions. *Magn Reson Med*. Oct 2008;60(4):895-907. doi:10.1002/mrm.21728
160. Huo D, Wilson DL. Robust GRAPPA reconstruction and its evaluation with the perceptual difference model. *J Magn Reson Imaging*. Jun 2008;27(6):1412-20. doi:10.1002/jmri.21352
161. Park J, Zhang Q, Jellus V, Simonetti O, Li D. Artifact and noise suppression in GRAPPA imaging using improved k-space coil calibration and

variable density sampling. *Magn Reson Med*. Jan 2005;53(1):186-93. doi:10.1002/mrm.20328

162. Chen Y, Lee GR, Wright KL, et al. Free-breathing liver perfusion imaging using 3-dimensional through-time spiral generalized autocalibrating partially parallel acquisition acceleration. *Invest Radiol*. Jun 2015;50(6):367-75. doi:10.1097/RLI.0000000000000135

163. Arunachalam A, Samsonov A, Block WF. Self-calibrated GRAPPA method for 2D and 3D radial data. *Magn Reson Med*. May 2007;57(5):931-8. doi:10.1002/mrm.21223

164. Wong ST, Roos MS. A strategy for sampling on a sphere applied to 3D selective RF pulse design. *Magn Reson Med*. Dec 1994;32(6):778-84. doi:10.1002/mrm.1910320614

165. Chieh SW, Kaveh M, Akçakaya M, Moeller S. Self-calibrated interpolation of non-Cartesian data with GRAPPA in parallel imaging. *Magn Reson Med*. 05 2020;83(5):1837-1850. doi:10.1002/mrm.28033

166. Sotiropoulos SN, Moeller S, Jbabdi S, et al. Effects of image reconstruction on fiber orientation mapping from multichannel diffusion MRI: reducing the noise floor using SENSE. *Magn Reson Med*. Dec 2013;70(6):1682-9. doi:10.1002/mrm.24623

167. Roemer PB, Edelstein WA, Hayes CE, Souza SP, Mueller OM. The NMR phased array. *Magn Reson Med*. Nov 1990;16(2):192-225. doi:10.1002/mrm.1910160203

168. Piccini D, Littmann A, Nielles-Vallespin S, Zenge MO. Spiral phyllotaxis: the natural way to construct a 3D radial trajectory in MRI. *Magn Reson Med*. Oct 2011;66(4):1049-56. doi:10.1002/mrm.22898

169. Jackson JI, Meyer CH, Nishimura DG, Macovski A. Selection of a convolution function for Fourier inversion using gridding [computerised tomography application]. *IEEE Trans Med Imaging*. 1991;10(3):473-8. doi:10.1109/42.97598

170. Wang Z, Bovik AC, Sheikh HR, Simoncelli EP. Image quality assessment: from error visibility to structural similarity. *IEEE Trans Image Process*. Apr 2004;13(4):600-12. doi:10.1109/tip.2003.819861
171. Piccini D, Demesmaeker R, Heerfordt J, et al. Deep Learning to Automate Reference-Free Image Quality Assessment of Whole-Heart MR Images *Radiology: Artificial Intelligence*. 2020;2(3)
172. Etienne A, Botnar RM, Van Muiswinkel AM, Boesiger P, Manning WJ, Stuber M. "Soap-Bubble" visualization and quantitative analysis of 3D coronary magnetic resonance angiograms. *Magn Reson Med*. Oct 2002;48(4):658-66. doi:10.1002/mrm.10253
173. Akçakaya M, Nam S, Hu P, et al. Compressed sensing with wavelet domain dependencies for coronary MRI: a retrospective study. *IEEE Trans Med Imaging*. May 2011;30(5):1090-9. doi:10.1109/TMI.2010.2089519
174. Hosseini SAH, Zhang C, Weingärtner S, et al. Accelerated coronary MRI with sRAKI: A database-free self-consistent neural network k-space reconstruction for arbitrary undersampling. *PLoS One*. 2020;15(2):e0229418. doi:10.1371/journal.pone.0229418
175. Henningsson M, Prieto C, Chiribiri A, Vaillant G, Razavi R, Botnar RM. Whole-heart coronary MRA with 3D affine motion correction using 3D image-based navigation. *Magn Reson Med*. Jan 2014;71(1):173-81. doi:10.1002/mrm.24652
176. Aitken AP, Henningsson M, Botnar RM, Schaeffter T, Prieto C. 100% Efficient three-dimensional coronary MR angiography with two-dimensional beat-to-beat translational and bin-to-bin affine motion correction. *Magn Reson Med*. Sep 2015;74(3):756-64. doi:10.1002/mrm.25460
177. Correia T, Ginami G, Cruz G, et al. Optimized respiratory-resolved motion-compensated 3D Cartesian coronary MR angiography. *Magn Reson Med*. 12 2018;80(6):2618-2629. doi:10.1002/mrm.27208
178. Munoz C, Cruz G, Neji R, Botnar RM, Prieto C. Motion corrected water/fat whole-heart coronary MR angiography with 100% respiratory efficiency. *Magn Reson Med*. 08 2019;82(2):732-742. doi:10.1002/mrm.27732

179. Fuin N, Bustin A, Küstner T, et al. A multi-scale variational neural network for accelerating motion-compensated whole-heart 3D coronary MR angiography. *Magn Reson Imaging*. 07 2020;70:155-167. doi:10.1016/j.mri.2020.04.007
180. Shu Y, Riederer SJ, Bernstein MA. Three-dimensional MRI with an undersampled spherical shells trajectory. *Magn Reson Med*. Sep 2006;56(3):553-62. doi:10.1002/mrm.20977
181. Gurney PT, Hargreaves BA, Nishimura DG. Design and analysis of a practical 3D cones trajectory. *Magn Reson Med*. Mar 2006;55(3):575-82. doi:10.1002/mrm.20796
182. Irarrazabal P, Nishimura DG. Fast three dimensional magnetic resonance imaging. *Magn Reson Med*. May 1995;33(5):656-62. doi:10.1002/mrm.1910330510
183. Turley DC, Pipe JG. Distributed spirals: a new class of three-dimensional k-space trajectories. *Magn Reson Med*. Aug 2013;70(2):413-9. doi:10.1002/mrm.24475
184. John H, Kevin W, Jessica B, et al. Free-running SIMilarity-Based Angiography (SIMBA) for simplified anatomical MR imaging of the heart. 2020Located at: https://arxiv.org/ftp/arxiv/papers/2007/2007.06544.pdf.
185. Usman M, Atkinson D, Odille F, et al. Motion corrected compressed sensing for free-breathing dynamic cardiac MRI. *Magn Reson Med*. Aug 2013;70(2):504-16. doi:10.1002/mrm.24463
186. Heye AK, Culling RD, Valdés Hernández MeC, Thrippleton MJ, Wardlaw JM. Assessment of blood-brain barrier disruption using dynamic contrast-enhanced MRI. A systematic review. *Neuroimage Clin*. 2014;6:262-74. doi:10.1016/j.nicl.2014.09.002
187. O'Connor JP, Jackson A, Parker GJ, Roberts C, Jayson GC. Dynamic contrast-enhanced MRI in clinical trials of antivascular therapies. *Nat Rev Clin Oncol*. Feb 2012;9(3):167-77. doi:10.1038/nrclinonc.2012.2
188. Tofts PS, Brix G, Buckley DL, et al. Estimating kinetic parameters from dynamic contrast-enhanced T(1)-weighted MRI of a diffusable tracer: standardized quantities and symbols. *J Magn Reson Imaging*. Sep

1999;10(3):223-32. doi:10.1002/(sici)1522-2586(199909)10:3<223::aid-jmri2>3.0.co;2-s

189. Law M, Yang S, Babb JS, et al. Comparison of cerebral blood volume and vascular permeability from dynamic susceptibility contrast-enhanced perfusion MR imaging with glioma grade. *AJNR Am J Neuroradiol*. May 2004;25(5):746-55.

190. Yang S, Law M, Zagzag D, et al. Dynamic contrast-enhanced perfusion MR imaging measurements of endothelial permeability: differentiation between atypical and typical meningiomas. *AJNR Am J Neuroradiol*. Sep 2003;24(8):1554-9.

191. Cramer SP, Simonsen H, Frederiksen JL, Rostrup E, Larsson HB. Abnormal blood-brain barrier permeability in normal appearing white matter in multiple sclerosis investigated by MRI. *Neuroimage Clin*. 2014;4:182-9. doi:10.1016/j.nicl.2013.12.001

192. Montagne A, Barnes SR, Sweeney MD, et al. Blood-brain barrier breakdown in the aging human hippocampus. *Neuron*. Jan 2015;85(2):296-302. doi:10.1016/j.neuron.2014.12.032

193. El Khouli RH, Macura KJ, Jacobs MA, et al. Dynamic contrast-enhanced MRI of the breast: quantitative method for kinetic curve type assessment. *AJR Am J Roentgenol*. Oct 2009;193(4):W295-300. doi:10.2214/AJR.09.2483

194. Rosenkrantz AB, Lim RP, Haghighi M, Somberg MB, Babb JS, Taneja SS. Comparison of interreader reproducibility of the prostate imaging reporting and data system and likert scales for evaluation of multiparametric prostate MRI. *AJR Am J Roentgenol*. Oct 2013;201(4):W612-8. doi:10.2214/AJR.12.10173

195. Cramer SP, Larsson HB. Accurate determination of blood-brain barrier permeability using dynamic contrast-enhanced T1-weighted MRI: a simulation and in vivo study on healthy subjects and multiple sclerosis patients. *J Cereb Blood Flow Metab*. Oct 2014;34(10):1655-65. doi:10.1038/jcbfm.2014.126

196. Rosenkrantz AB, Geppert C, Grimm R, et al. Dynamic contrast-enhanced MRI of the prostate with high spatiotemporal resolution using compressed sensing, parallel imaging, and continuous golden-angle radial sampling:

preliminary experience. *J Magn Reson Imaging*. May 2015;41(5):1365-73. doi:10.1002/jmri.24661
197. Awate SP, DiBella EVR. Spatiotemporal dictionary learning for undersampled dynamic MRI reconstruction via joint frame-based and dictionary-based sparsity. presented at: 9th IEEE International Symposium on Biomedical Imaging; 2012;
198. Caballero J, Price AN, Rueckert D, Hajnal JV. Dictionary learning and time sparsity for dynamic MR data reconstruction. *IEEE Trans Med Imaging*. Apr 2014;33(4):979-94. doi:10.1109/TMI.2014.2301271
199. Barger AV, Block WF, Toropov Y, Grist TM, Mistretta CA. Time-resolved contrast-enhanced imaging with isotropic resolution and broad coverage using an undersampled 3D projection trajectory. *Magn Reson Med*. Aug 2002;48(2):297-305. doi:10.1002/mrm.10212
200. Haider CR, Hu HH, Campeau NG, Huston J, Riederer SJ. 3D high temporal and spatial resolution contrast-enhanced MR angiography of the whole brain. *Magn Reson Med*. Sep 2008;60(3):749-60. doi:10.1002/mrm.21675
201. Kobayashi N. Evaluation of UTE for improved contrast enhanced DCE MRI at 7T; at proceedings of ISMRM. 2018;

Appendix A

Tuning CS parameters

For the whole-heart coronary MRI experiment in Chapter 4, the CS reconstruction was implemented using ADMM, requiring tuning of two parameters. One is the parameter for TV regularization in the proximal operation, which is denoted by λ in Eq. 8. The other parameter is a penalty parameter for data fidelity, which is denoted by β. After the visual inspection of different CS images corresponding to different choices of these two parameters, along with the corresponding NRMSE and SSIM quantitative metrics with respect the reference, the appropriate selection of λ and β are empirically picked. This appendix shows various CS reconstructions that correspond to different choices of parameters λ and β. The goal is to verify the appropriateness of the selected parameters. The inspected ranges of λ and β are $0.001 \cdot \|\mathbf{E}^*\mathbf{y}\|_\infty \leq \lambda \leq 0.5 \cdot \|\mathbf{E}^*\mathbf{y}\|_\infty$ and $0.01 \leq \beta \leq 2$. $\mathbf{E}^*\mathbf{y}$ is implemented with the gridding image of the undersampled data. For each CS reconstruction, the NRMSE and SSIM are calculated with respect to the reference image over the volume of the whole heart.

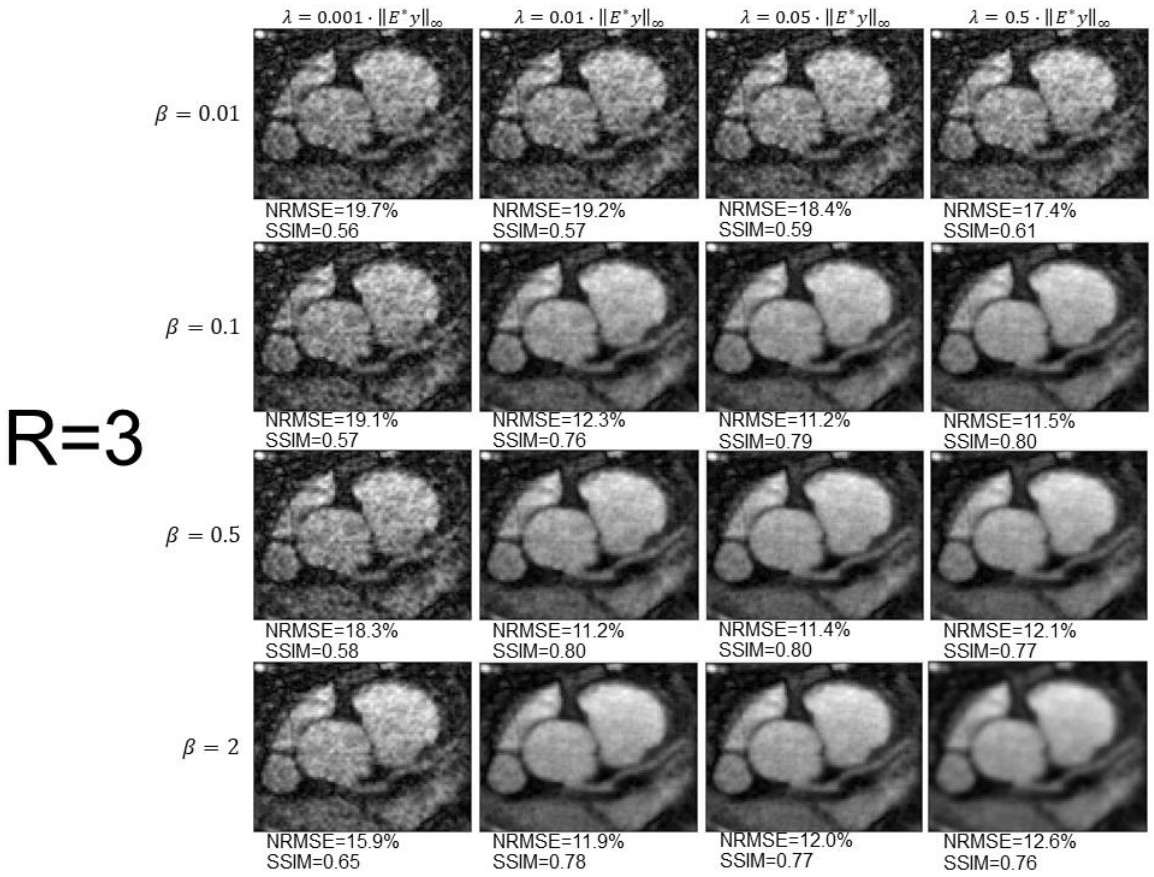

Figure A.1: The 16 CS reconstructions at R=3 corresponding to 16 total combinations of four different λ and four different β.

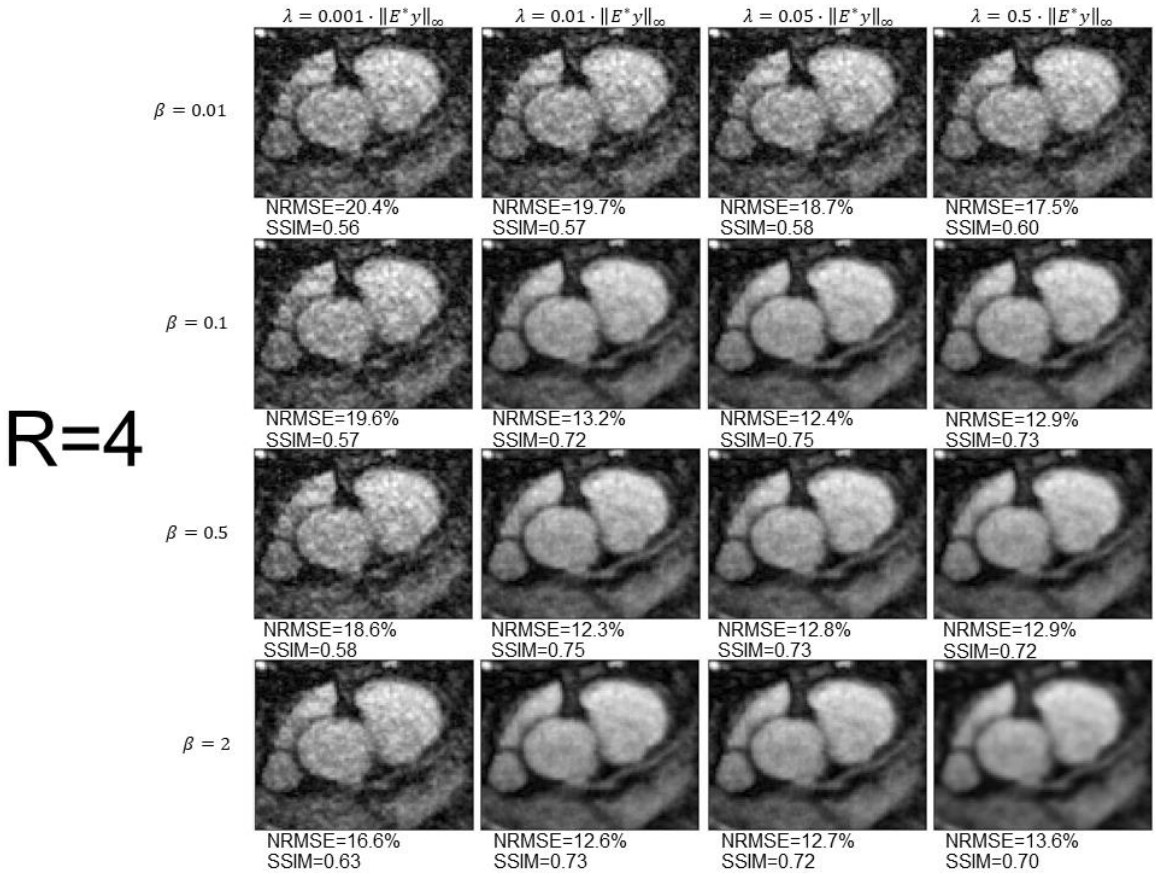

Figure A.2: The 16 CS reconstructions at R=4 corresponding to 16 total combinations of four different λ and four different β.

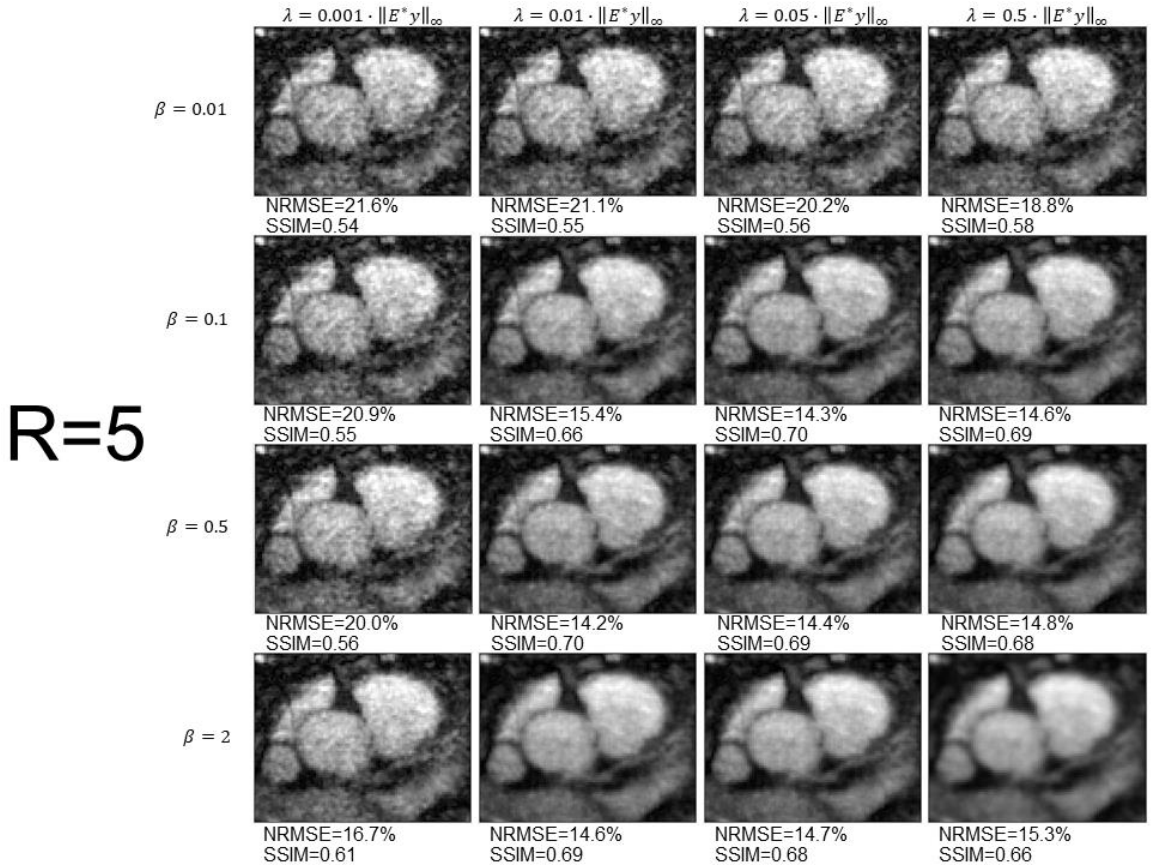

Figure A.3: The 16 CS reconstructions at R=5 corresponding to 16 total combinations of four different λ and four different β.

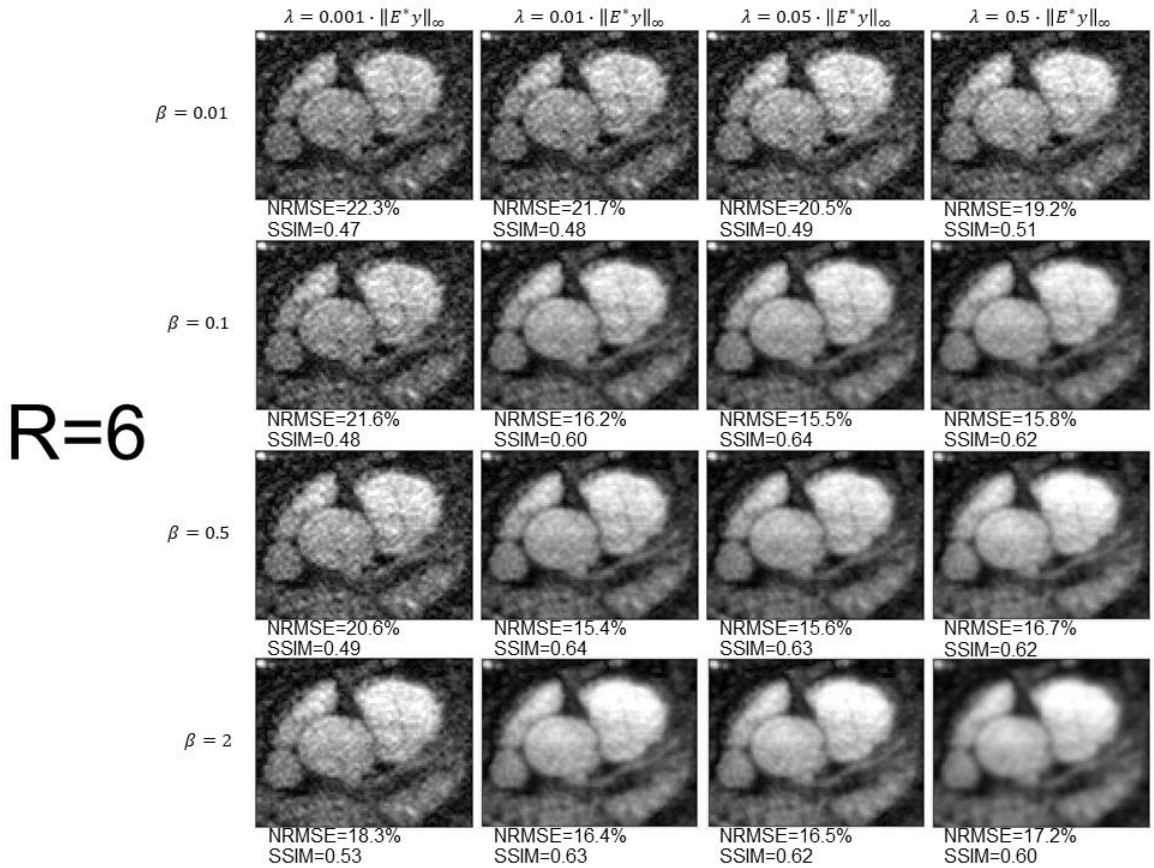

Figure A.4: The 16 CS reconstructions at R=6 corresponding to 16 total combinations of four different λ and four different β.

The ranges $0.05 \cdot \|\mathbf{E}^*\mathbf{y}\|_\infty \leq \lambda \leq 0.5 \cdot \|\mathbf{E}^*\mathbf{y}\|_\infty$, for $\beta = 0.1$, and $0.01 \cdot \|\mathbf{E}^*\mathbf{y}\|_\infty \leq \lambda \leq 0.1 \cdot \|\mathbf{E}^*\mathbf{y}\|_\infty$, for $\beta = 0.5$ are found to produce CS reconstructions that are visually and quantitatively (evaluated using NRMSE and SSIM) better among all images reconstructed with different parameters within the inspected ranges. This finding is consistent across each of the four rates R={3,4,5,6}. Low λ values produce noisy images with artifacts, while high λ values produce blurred images. The same trend is also observed when varying the value of β. The CS reconstruction parameters

are empirically selected as $\lambda = 0.02 \cdot \|\mathbf{E}^{*}\mathbf{y}\|_{\infty}$ and $\beta = 0.5$, since they are within the range that produces reasonable reconstructions.